The Scientific Institute for Advanced Training and Studies

Experimental and Theoretical NANOTECHNOLOGY

Vol. 1, No. 1, 2017

Yarub Al-Douri
Editor-in-Chief

e-ISSN: 2590-4132

Contact us

Experimental and Theoretical NANOTECHNOLOGY

Prof. Dr. Yarub Al-Douri; Founding Editor-in-Chief :editor.etn@siats.co.uk

http://etn.siats.co.uk

Experimental and Theoretical NANOTECHNOLOGY
http://etn.siats.co.uk/

Experimental and Theoretical NANOTECHNOLOGY

VOL. 1, NO. 1, 2017

e-ISSN 2590-4132

2017

Experimental and Theoretical NANOTECHNOLOGY

Experimental and Theoretical NANOTECHNOLOGY is a multidisciplinary peer-reviewed international journal published four issues a year. It includes specialized research papers, short communications, reviews and selected conference papers in special issues on the characterization, synthesis, processing, structure and properties of different principles and applications of NANOTECHNOLOGY; with focus on advantageous achievements and applications for the specialists in engineering, chemistry, physics and materials science.

Experimental and Theoretical NANOTECHNOLOGY covers and publishes all aspects of fundamental and applied researches of experimental and theoretical nanoscale technology dealing with materials synthesis, processing, nanofabrication, NANO probes, spectroscopy, properties, biological systems, nanostructures, NANO electronics, Nano-optics, NANO-mechanics, NANO-devices, NANO biotechnology, nanomedicine, Nano toxicology within the scope of the journal. Experimental and Theoretical NANOTECHNOLOGY aims to acquire the recent and outstanding researches for the benefit of the human being.

Exp. Theo. NANOTECHNOLOGY 1 **(2017)** 01 – 12

Experimental and Theoretical
NANOTECHNOLOGY
http://etn.siats.co.uk/

The effect of additives on behavior of the high temperature $La_xY_{1-x}Ba_2Cu_3O_{7-\delta}$ superconductor

Alhuthari Abdulbaqi Ali1, Widad Mahmood Faisal1, Salwan K. J. Al-Ani2,*

1Department of Electronic & Communicatio, Faculty of Engenering & Petroleum,
Hadramout University, Hadramout, Yemen
2Department of Physics, College of Science, University of Baghdad, Baghdad, Iraq
*) Email: salwan_kamal@yahoo.com

Received 28 May 2015; Revised 9 July 2015; Accepted 16 Feb. 2016

A series of ceramic superconductor compounds with the composition $La_xY_{1-x}Ba_2Cu_3O_{7-\delta}$ are prepared by solid state reaction from the principle routs like La_2O_3, $BaCO_3$ and CuO with high purity 99.99%. Different measurement are made to show the improvement in high phase superconductor such as resistivity measurement and the X-ray diffraction (XRD). When (x=0.20 and 0.80; x=0.40 and 0.60) an orthorhombic phase is appeared with lattice constants (a= 3.844 Å, b=3.912 Å, c=11.839 Å) and (a= 3.871 Å, b=3.881 Å, c=11.748Å), respectively. This emphasizes the formation of a high temperature superconducting phase. At x=0.5 a phase is changed to a tetragonal where the superconductivity is lost. From the resistivity measurement, the highest (Tc) value is found equals to (97K) for (x=0.20 and x=0.80) comparable with the YBCO-compound which does not normally exhibited Tc-value greater than (95K). The increase in Tc-value may be attributed to the amount of (La) and / or the oxygen content in the mixture which both influence the properties of the compound and are essential for the superconductivity phase.

Keywords: High temperature superconductor; $La_xY_{1-x}Ba_2Cu_3O_{7-\delta}$; X-ray diffraction; Resistivity measurement; Critical temperature.
PACS: 74.25.-q; 61.05.cp; 84.37.+q; 74.10.+v; 74.62.-c.

1. Introduction

The detection of the so-called High Temperature Superconductor (HTS) in 1986 by Bednorz and Muller [1] dramatically changed the prospect of electrical power applications of superconductors, because of the significantly increased critical temperature, T_C, in which the employment of a more economical cryogen, liquid nitrogen becomes possible. Between 1987 and 1993, T_C is raised from 92 K as revealed in YBa_2Cu_3Ox (YBCO) [2]. Moreover 130 K is ~~as~~ demonstrated in $Hg_2Ba_2Ca_2Cu_3Oy$ [3]. Meanwhile, extensive efforts have been directed to develop practical HTS conductors with high current carrying capability. First, concentrating on Bi-2223 ($Bi_2Sr_2Ca_2Cu_3O_z$) and recently on YBCO-123 based coated conductor, referred to as ‘‘2nd generation conductor’’. With low losses and high current carrying capability, HTS conductors allows electrical devices to be built with higher efficiency and higher power density. It also enables novel devices such as Superconducting Magnetic Energy Storage (SMES), magnetic bearings, fault current limiters and switches [4]. Furthermore, HTS offers environmental advantages; oil free transformers and devices with low magnetic field leakage. In the hope of a large scale HTS application in electrical power industry, significant public and private programmers have been initiated both to accelerate conductor development and to build prototypes in the USA, Europe, and Japan.

HTS represents a new class of conductor with unique properties, which not only allows electric power devices to be more compact but also enables new applications. The conductors developed so far have enabled various power device prototypes, such as power cables [6-8], transformers [9,10], motors [11,12], and Superconducting Fault Current Limiters (SCFCL) [13-15].

As compared with common superconducting materials such as $YBa_2Cu_3O_Y$, La-based high-temperature superconducting (HTSC) possess some attracting features, such as high superconducting critical temperature (T_C), high critical current density *(*J_C*)*, very low microwave surface resistance (R_s) and a good stability in moisture [16–20]. All of these properties merit potential superiority of La-based thin-film devices for electronic applications, ranging from superconducting quantum interference devices (SQUIDs) to superconducting microwave resonators and also other passive devices [21–26]. The effects of partial substitution of Y by La –atom on the growth mechanism and superconducting properties will be studied for the component $La_xY_{1-x}Ba_2Cu_3O_{7-\delta}$ at x=0, 0.20, 0.40, 0.50, 0.60 and 0.80 .

2. Experimental Procedure

The samples are prepared by using the standard solid-state reaction technique. The detailed procedures for the sample preparation are as follows; pure cation oxides of Y_2O_3 (99.995%), La_2O_3 (99.99%), $BaCO_3$ (99.99%), and CuO (99%) are weighted and mixed according to the chemical formula of $YBa_2Cu_3O_{7-y}$ (YBCO) and $La_xY_{1-x}Ba_2Cu_3O_{7-\delta}$ with x=0, 0.20, 0.40, 0.50, 0.60 and 0.80.

In order to make, the specimens mixture is prepared by homogeneously mixing and grinding prescribed amounts of powders into a gate mortar. Appropriate amounts of these powders are mixed with alumna mortar and pestle for (2 hours) in 2- propanole and dried. They are put into a furnace (Nabartherm-N11/R) and calcined at 930°C in air for 48 hrs. This process is repeated three times. Then, the final step of the sample preparation is undergone to high temperature treatment that leads the particles to join together and gradually reduce the volume of pore space between them. The powder is compacted into a pellet shape with a certain pressure. After that, the powder particles will then be in contact with one another at numerous sites, with significant amount of pore space between the particles. In order to reduce the boundary energy, atoms diffuse to the boundaries, permitting the particles to be bound together and eventually causing shrinkage in the pores. However, if sintering is carried out for a long time the pores may be eliminated and the material becomes dense.

The calcined powders are pulverized and reground pelletized into disk-shaped pellets. The die has a stainless steel cylinder of 0.5 cm (13 mm) diameter and 1.5-1.8 mm thick using manually hydraulic press RAKIN-EIMER, under a pressure of 8 ton/cm^2 (0.6 Gp). The programming data for this process includes; the rate of heating (60C°/hour) up to (930 °C) for 30 hours with the flow of oxygen gas of about 1.25 L/min and then with slow rate of cooling (30 °C/hours). The temperature is, afterwards, decreased down to about 550°C with 4 °C /min and kept at this level for 12 hrs in oxygen flow to enhance the value of **δ** to reach the content of oxygen atoms in the samples to about (6.85) before returning to a room temperature. Finally, the products are cooled down to a room temperature.

2.1. X-Ray diffraction

The structural characterization is performed by X-ray diffraction (XRD). While the X-ray powder diffractometry is generally dealing exclusively with crystalline (order) materials. X-ray patterns are used for initial identification of lattice type as the unit of crystal structure and the building black for the materials with acknowledge of the chemical composition ionic size, lattice parameters, structure model can be built X-Ray diffraction pattern can be utilized to determine the phase present in the sample by observing the intensity peaks in relation to its (hkl) values. Based on the determination of Miller indices, hkl, and the lattice parameters for all the orthogonal crystal systems are calculated as the following. For cubic system, a=b=c

$$\frac{1}{d_{hkl}^{2}} = \frac{h^{2}+k^{2}+l^{2}}{a^{2}} \qquad (1)$$

For tetragonal system, $\mathrm{a} = \mathrm{b} \neq \mathrm{c}$

$$\frac{1}{d_{hkl}^{2}} = \frac{h^{2}+k^{2}}{a^{2}} + \frac{l^{2}}{c^{2}} \qquad (2)$$

and fororthorhombic system, $\mathrm{a} \neq \mathrm{b} \neq \mathrm{c}$

$$\frac{1}{d_{hkl}^{2}} = \frac{h^{2}}{a^{2}} + \frac{k^{2}}{b^{2}} + \frac{l^{2}}{c^{2}} \qquad (3)$$

In this work, (XRD) type PHILIPS with the following features; the source Cu KαI, current 20 mA, Voltage 40 kV and λ=1.5405 Å are used. The X-ray chart and ASTM-data [27] are used in a computer program to analysis the X-ray data in order to refine the structure of the sample conducted in this study and to obtain the lattice constants.

2.2. Sample Testing

The critical temperature of the superconducting sample is measured by using the four-point probe technique which is considered as a suitable method for studying the electrical behavior of superconducting materials. In this method, a small current passed through a sample and the voltage drop across it. The terminals distinct from those utilized for passing the main part of the current through the specimen, where voltage drop in both leads and contacts are the electrical contact to the sample which are made with fine copper wires adhered with silver paste. The cryostat system is used for the measurement of critical resistivity of the sample with the present of a liquid Nitrogen. The cryostat is joined to a rotary pump to get a pressure of ~10^{-2} mbar inside the cryostat.

3. Result and Discussions

3.1. Structure properties of $La_xY_{1-x}Ba_2Cu_3O_{7-\delta}$

All samples of partial substitution of Y by La –atom are examined by powder XRD and the typical XRD –2*θ* patterns are presented in Fig's 1, 2, 3, and 4, respectively. These results indicate that there are a good crystalline which textured with the *c*-axis perpendicular to the surface of the substrate. The four sharp peaks are consistent in intensity and shifted by 90° from one peak to another indicating the fourfold symmetry of the La-2212 crystal. To examine the presence of superconductivity phase, the structure nature of orthorhombic phase for all samples under study with (x=0, 0.20, 0.40, 0.60 and 0.80) is investigated.

The X-ray analyses show that all the compounds exhibit essentially c-axis oriented with good crystalline may not relate closely to the initial substrate conditions. Due to La substitution in Y with some modifications in the peaks appear represented by their intensity or positions .The effect of substitution of La on the Y with the concentration (x=0.20, x=0.80) is presented in Fig. 1. When substituting Y by La for the component $La_xY_{1-x}Ba_2Cu_3O_{7-\delta}$ for x=0, 0.20, 0.40, 0.50, 0.60, 0.80 show a gradual transfer the orthorhombic phase to a tetragonal at x=0.50**.**

When x=0.20 and x=0.8, the HTS exhibits an orthorhombic phase with a lattice cell constants a= 3.844 Å, b=3.912 Å, C=11.839 Å as shown in Fig. 1. The lattice parameters, unit cell volume and orthorhombicity are listed in Table I. The increase in the c parameter is significant and is indicative of the Y replacement by La. This, however, does not guarantee the absence of partial Ba substitution by La. A smaller unit cell volume for x=0.1 is similar to the results of Liang et al. [28] who observed a decreasing trend in the unit cell volume for increasing Ba substitution by La.

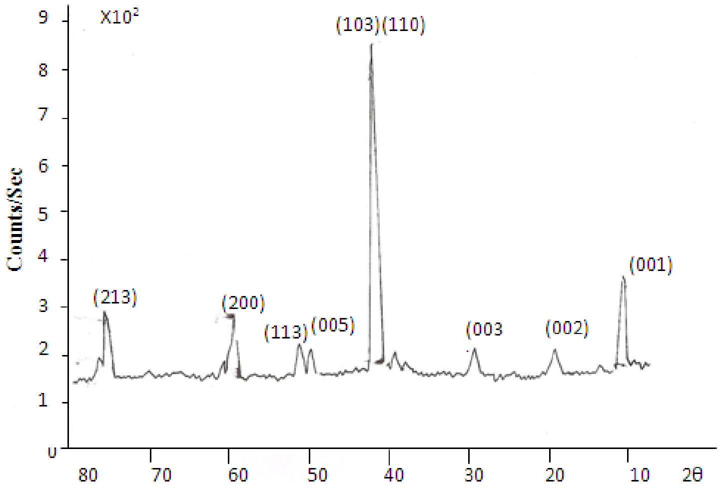

Figure. 1: X-ray diffraction for the component $La_xY_{1-x}Ba_2Cu_3O_{7-\delta}$ for x=0.2, x=0.8 with oxygen vacuum in temperature 930 °C.

when x=0.4 and x=0.6, it exhibits an orthorhombic phase with a lattice cell parameters; a= 3.871 Å, b=3.881 Å, c=11.748 Å as shown in Fig. 2.

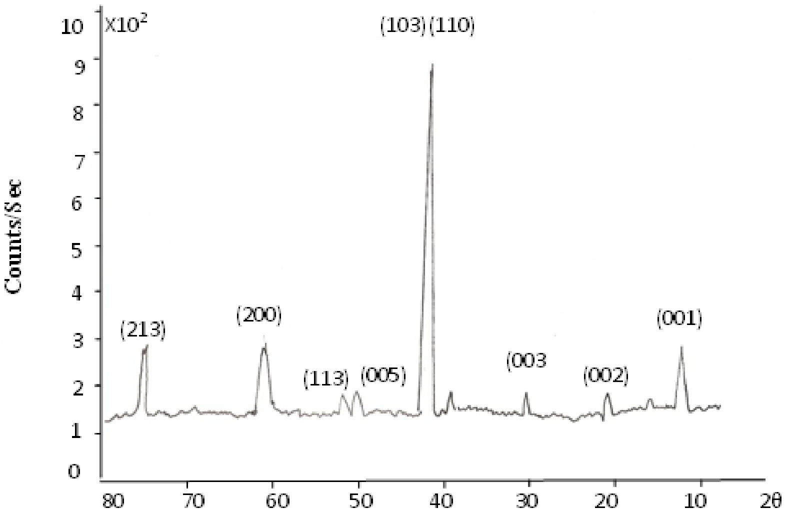

Figure. 2: X-ray Diffraction for the component $La_xY_{1-x}Ba_2Cu_3O_{7-\delta}$ for x=0.4, x=0.6 with oxygen vacuum in temperature 930 °C.

At last x=0.50 is orthorhombic phase lattice cell a=b= 3.876 Å, c=11.743 Å as shown in Fig. 3.

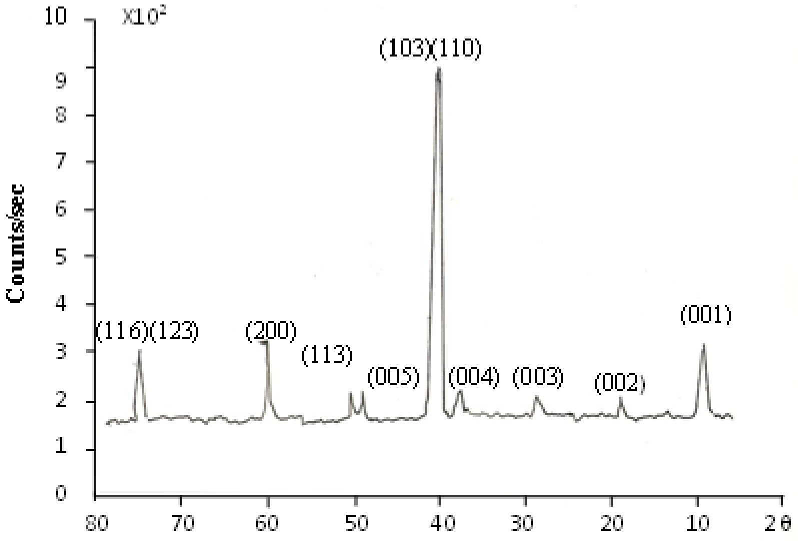

Figure. 3: X-ray Diffraction for the component $La_xY_{1-x}Ba_2Cu_3O_{7-\delta}$ for x=0.5 with oxygen vacuum in temperature 930 °C.

While the x=0.5 sample shows loss of superconductivity, this behavior, similar to that of $Y(La_xBa_{1-x})Cu_3O_7$ samples reported earlier [28,29], which consists of a decrease in T_c as x ($La_xY_{1-x}Ba_2Cu_3O_{7-\delta}$) is increased and a disappearance of superconductivity at x≈ 0.5. This similarity in the variation of superconducting properties with the lanthanum content suggests the possibility of lanthanum substitution for barium and the concomitant mixing of the La and Ba sites in our samples. From the neutron diffraction studies such a mixing is known to occur in $LaBa_2Cu_3O_7$ [30]. Thus, the behavior of the solid solutions seems to be guided by the substitution of La into the Ba sites along with the Y sites. When x=0, it gives the structure $YBa_2Cu_3O_{7-\delta}$ with lattice constants; a= 3.842 Å, b=3.912 Å, c=11.752 Å as shown in Fig. 4.

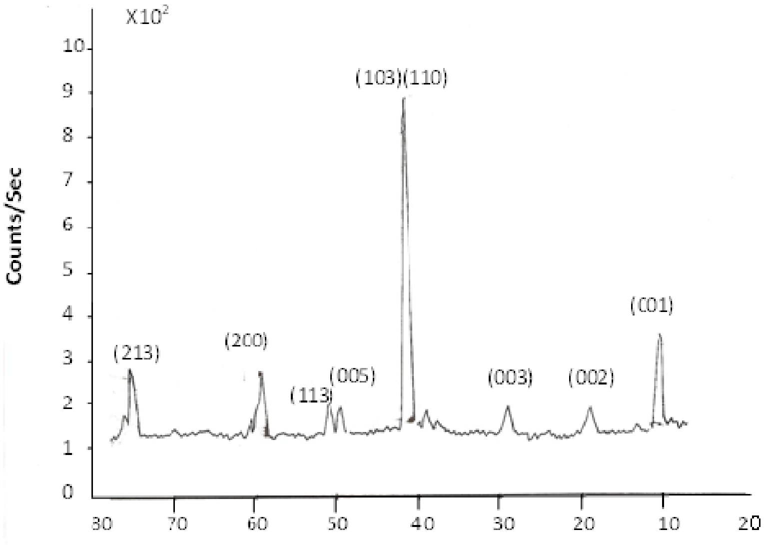

Figure. 4: X-ray Diffraction for the component $La_xY_{1-x}Ba_2Cu_3O_{7-\delta}$ for x=0 with oxygen vacuum in temperature 930 °C.

The X-ray diffraction pattern of this sample shows the splitting of the (200) and (005) reflections, though the resistivity behavior is still semiconducting. Thus, the importance of proper oxygen stoichiometry in addition to the orthorhombic structure for the occurrence of superconductivity in the 123 system is evident.

3.2. Resistivity properties of $La_xY_{1-x}Ba_2Cu_3O_{7-\delta}$

The zero field resistivity as a function of temperature for the nominal compositions $La_xY_{1-x}Ba_2Cu_3O_{7-\delta}$ (x = 0, 0.20 and 0.40) are shown in Fig's 5, 6 and 7 (the lower inset shows the resistivity over a larger range of temperature) measured by standard four probe method. The resistivity decreases monotonously with decreasing temperature and the onset of superconducting transition occurs at 95, 97 and 96 K for x = 0, x= 0.20 and x = 0.40 compositions respectively.

For x = 0.20 and x = 0.40, the transition is rather broad and the T_c values are approximate. This enhancement in Tc indicates that small amount of Yttrium is substituted at the La sites. The smaller size of Yttrium (atomic radius 180 pm) as compared to lanthanum (atomic radius 195 pm) leads to subtle changes in the bandwidth and this probably enhances the superconducting transition temperature. Nevertheless, in compositions with higher Yttrium ratio, the superconducting transition temperature decreases and the transition broadens which suggests the compositional dependence of Tc. whereas, at x=0.5 the composition is losing its superconductivity. It is known that a small changes in the crystalline structure of a high temperature cuprate superconductor (HTCS) produce large changes in its magnetic properties [31]. The structural changes are produced by chemical substitutions of cations or anions. Thus, altering the position and occupancy of the atoms situated in the superconducting planes CuO_2 and also leads to increasing (or decreasing) the superconducting critical temperature (Tc) .Indeed Luis et al [31] reported that by changing the oxygen content in the superconductor $YBa_2Cu_3O_7$ (YBCO-7) to ≤ 6.4, the occupancy of the oxygen situated in the Cu-O chains decreases and the crystalline structure changes from orthorhombic to tetragonal where the superconductivity is destroyed.

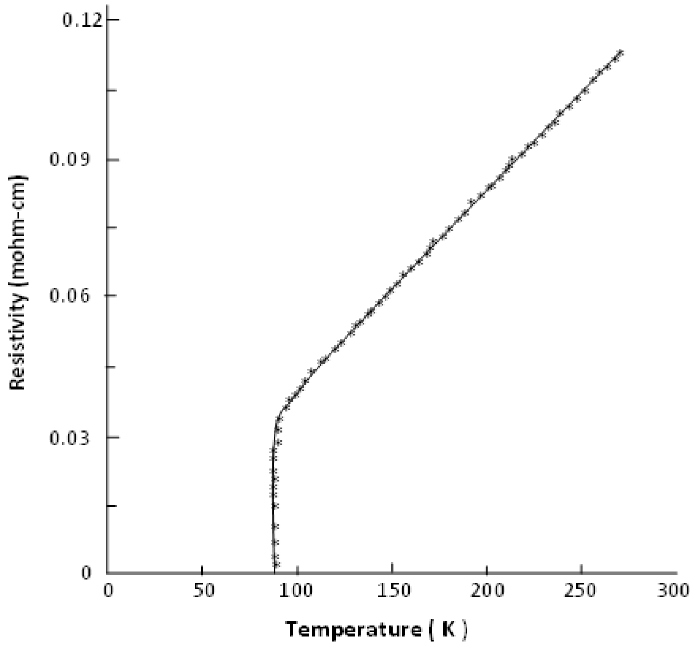

Figure. 5: The resistivity versus temperature for HTSC $La_xY_{1-x}Ba_2Cu_3O_{7-\delta}$.

The relation of resistivity vs. temperature curve for the concentration x=0 is shown in Fig. 5 with Tc=95K. While, the critical temperature is increased when the concentration x=0.2 and x=0.8; Tc = 97K and at x=0.4; Tc = 96 K as shown in Fig. 6.

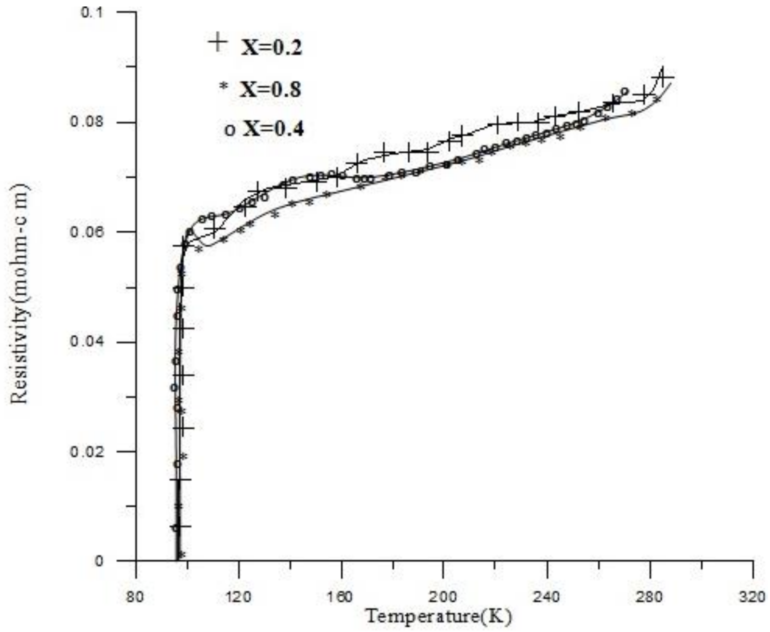

Figure. 6: The resistivity verus temperature for HTSC $La_xY_{1-x}Ba_2Cu_3O_{7-\delta}$ for x= 0.2, x=0.8

The resistivity dropped suddenly with concentration x=0.6 [Tc=83K], which is due to (La) substitution in the mixture and hence affects the Tc values as shown in Fig. 7. The values of Tc for different components of La_xY_1-x$Ba_2Cu_3O_{7-\delta}$ superconductor are listed in Table I. Ganapathi et al. [30] earlier found for $x \leq 0.5$ the La_xY_{1-x} $Ba_2Cu_3O_{7-\delta}$ system behaves like a pure Y_{123} superconducting oxide with Tc onset equal to 90 K. They obtained a maximum Tc = 94 K (zero resistance at 91 K) when x=0.1. For x > 0.5 they reported that the system starts to behave like a La_{123}. The changes in the values of the Tc in the present system are due to changes in oxygen sites in chains and levels of CuO. These changes depend on the partial compensation of (CuO_2). The difference in these sites has caused confusion in the paths of Cooper pairs.

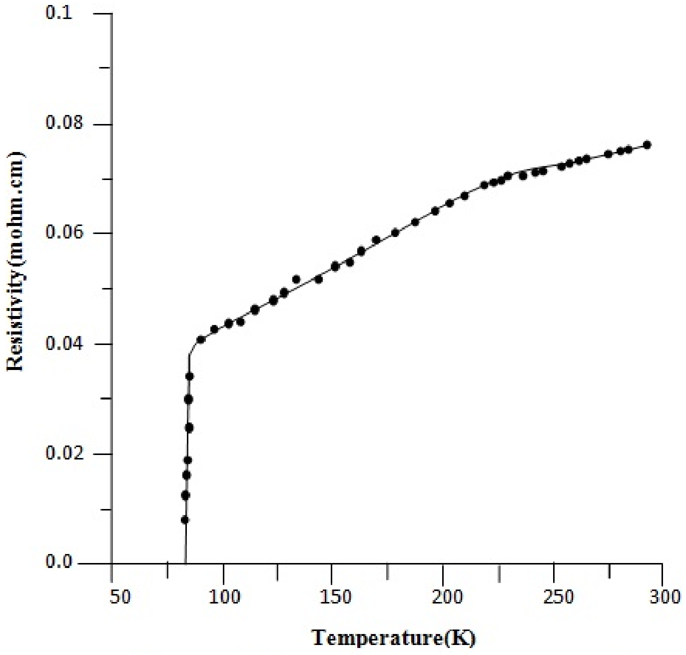

Figure. 7: The resistivity versus temperature for HTSC $La_xY_{1-x}Ba_2Cu_3O_{7-\delta}$ for x = 0.6

Table 1: The values of the lattice constants and the Tc for different components of $La_xY_{1-x}Ba_2Cu_3O_{7-\delta}$ superconductor.

Samples	**Tc (K) Onset**	**Lattice Constants**
$La_xY_{1-x}Ba_2Cu_3O_{7-\delta}$ for x=0	95 K	a= 3.842 b=3.912 c=11.752
$La_xY_{1-x}Ba_2Cu_3O_{7-\delta}$ for x=0.20	97 K	a= 3.844 b=3.912 c=11.839
$La_xY_{1-x}Ba_2Cu_3O_{7-\delta}$ for x=0.40	96 K	a= 3.871 b=3.881 c=11.748
$La_xY_{1-x}Ba_2Cu_3O_{7-\delta}$ for x=0.50	the component loses superconductivity	a=3.876 b= 3.876 c=11.743
$La_xY_{1-x}Ba_2Cu_3O_{7-\delta}$ for x=0.60	83K	a= 3.871 b=3.881 c=11.748
$La_xY_{1-x}Ba_2Cu_3O_{7-\delta}$ for x=0.80	97K	a= 3.844 b=3.912 c=11.839

4. Conclusions

This study shows that the growth mechanism and hence the resulting structural and superconducting properties are significantly affected by the substitution of Y - atoms by La atoms in $La_xY_{1-x}Ba_2Cu_3O_{7-\delta}$ compound for x=0, 0.2, 0.4, 0.5, 0.6, 0.8 and gradually transfer of the orthorhombic phase to the tetragonal phase when x=0.5. The present results have important implications that substitution can be used to control the microstructure and surface morphologies of YBCO compound. The superconductivity of the solid solution $La_xY_{1-x}Ba_2Cu_3O_{7-\delta}$ is a strong function of x. Lanthanum occupies both Y and Ba sites and the extent of Ba substitution by La controls the properties of the system. Samples with $0 \leq x \leq 0.8$ are orthorhombic with decreasing orthorhombicity as a function of x. The unit cell volume increases as x =0.2 and x=0.8. Two distinct behaviors are observed in the electrical characteristics of the solid solutions. For x =0.2 and x=0.8 the solid solution behaves similarly to the x=0 a member with a metallic behavior followed by a superconducting transition at Tc = 95 K. A slightly higher Tc= 96 K for the x=0.4 sample behavior followed by a superconducting transition at x=0.6, Tc= 83 K [26,32]. The orthorhombic structure and optimum oxygen content are found to be essential for the observation of superconductivity in the123 system. Interestingly, these two parameters are independent variables in the La-rich compounds, unlike the pure $Y_{1\,23}$ compound.

References

[1] G. Bednorz, K.A. Muller, Zeitschrift für Physik B **64** (1986) 189

[2] M.K. Wu, J.R. Ashburn, C.J. Torng, P.H. Hor, R.L. Meng, L. Gao, Q. Huang, C.W. Chu,Physical Review Letter **58** (1987) 908

[3] A. Schilling, M. Cartoni, J. Guo, H.R. Ott, Nature **363** (1993) 56

[4] B. Seeber, Handbook of Applied Superconductivity, OIP Publishing, Bristol (1998)

[5] M. Chen, L. Donzel, M. Lakner, W. Paul, Journal of the European Ceramic Society **24** (2004) 1815

[6] T. Masuda, Y. Ashibe, M. Watanabe, C. Suzawa, K. Ohkura, Hirose, Y. Takahashi, Physica C **372-376** (2002) 1580

[7] J.P. Stovall, J.W. Lue, J.A. Demko, P.W. Fisher, M.J. Gouge, R.A. Hawsey, J.W. Armstrong, R.L. Hugehy, J.C. Tolbert, Advances in Cryogenic Engineering **47** (2002) 591

[8] D. Willen, F. Hansen, M. Daumling, C.N. Rasmussen, C. Traeholt, S.D. Mikkelsen, Physica C **372-376** (2002) 1571

[9] R. Schlosser, M. Meinert, M. Leghissa, Ieee Transactions on Applied Superconductivity **2** (2003) 2348

[10] P.G. Therond, C. Levillain, J.F. Picard, B. Bugnon, H. Zeuger, S. Hornfeldt, T. Fogelberg,G. Papst, D. Bonmann, Proceding of 37th Cigre Session pp. 302 (1998)

[11] M. Frank, J. Frauenhofer, P. van Hasselt, W. Nick, H.-W. Neumueller, G. Nerowski, Ieee Transactions on Applied Superconductivity **13** (2003) 2120

[12] D. Madura, M. Richardson, D. Bushko, S. Kalsi, B. Gamble, The Applied Superconductivity Conference, Ieee (2002)

[13] W. Paul et al. Superconductor Science & Technology **10** (1997) 914

[14] W. Paul, M. Chen, M. Lakner, J. Rhyner, D. Braun, W. Lanz, Physica C **354** (2001) 27

[15] R. Witzmann, W. Schmidt, R. Volkmar, ETG-Fachberichte Band **85** (2001) 393

[16] D. S. Ginley, Tl-based HTSC films for microelectronic applications Thallium-Based High-Temperature Superconductors. Ed. A. M. Hermann and S. V Yakhmi (New York: Marcel Dekker) chapter 9 (1993)

[17] A.P. Bramley, J. D. O’Connor, C. R. M. Grovenor, Supercond. Sci. Technol. **12** (1999) R57

[18] H. Schneidewind, M. Manzel, G. Bruchlos, K. Kirsch, Supercond. Sci. Technol. 14 (2001) 200

[19] S. Huber, M. Manazel, H. Bruchlos, S. Hensen, G. Muller, Physica C **244** (1995) 337

[20] W. L. Holstein, L. A. Parisi, C. Wilker , R. B. Flippen, Appl. Phys. Lett. **60** (1992) 2014

[21] Y. F. Chen, Z. G. Ivanov, E. A. Stepantsov, A. Ya. Tzalenchuk, S. Zarembinski, T. Claeson, L-G. Johansson, J. Appl. Phys. **79** (1996) 9221

[22] W. L. Holstein, L. A. Parisi, Z-Y. Shen, C. Wilker, M. S. Brenner, J. S. Martens J. Supercond. **6** (1993) 191

[23] A. Cassinese, A. Andreone, E. Di Gennaro, G. Pica, R. Vaglio, G. Malandrino, L. M. S. Perdicaro, I. L. Fragala, C. Granata, Supercond. Sci. Technol. **14** (2001) 406

[24] M. Barra, A. Cassinese, I. Fragala, M. Kusunoki, G. Malandrino, T. Nakaggawa, L. Perdicaro, K. Sato, S. Oshima, R. Vaglio, Supercond. Sci. Technol. **15** (2002) 581

[25] D. Face, M. Frank, J. Robert, B. Likie, S. Mark, W. Charles, IEEE Trans. Appl. Supercond. **9** (1999) 2492

[26] D. S. Ginley, E. L. Venturini, C. P. Tigges, T. E. Zipperian, R. J. Baughman, J. C. Barbour, B. Morosin, Physica C **185** (1991) 2275

[27] J. Xiaoping, Z. Xiaobiao, P. Dexing, Q. Hongbo, Y. Zhougjin, Y. Huafeng, Z. Xizhang, L. Shuzhi, Q. Guiwen; J. Phys. C, Solid state Physics **20** (1987) L533

[28] R. Liang, M. Itoh, T. Nakamura and R. Aoki, Physica C **157** (1989) 83

[29] T.C. Huang, Y. Tokura, J.B. Torrance, A.I. Nazzal and R. Karimi, Appl. Phys. Lett. **52** (1988) 1901

[29] A. Sequeria, H. Rajagopal, L. Ganapathi and C.N.R. Rao, J. Solid State Chem. **76** (1988) 235

[30] L. Ganapathi, Ashok Kumar and J. Narayan, Fundamental Properties and Novel Materials, Vol. 169, 561-564, Proceeding of Materials Research Society (1989)

[31] V. Luis De Los Santos, D. Angel Bustamante, J. C. Gonzalez, L. Juan Feijoo, A. Ana Osorio, T. Mitrelias, Y. Majima, Crispin H.W. Barnes, The Open Superconductivity Journal **2** (2010) 19

[32] A. Manthiram, X.X. Tang, J. B. Goodenough, Phys. Rey. B **37** (1988) 3734

Exp. Theo. NANOTECHNOLOGY 1 **(2017)** 13 – 22

Experimental and Theoretical NANOTECHNOLOGY
http://etn.siats.co.uk/

1Tunable carbon quantum dots from starch via microwave assisted carbonization

L. A. Adams, K. A. Fagbenro-Owoseni*

Department of Chemistry, University of Lagos, Lagos, Nigeria
*) E-mail: ladams@unilag.edu.ng

Received 16 July 2015; Revised 26 July 2015; Accepted 28 Oct. 2016

Tunable luminescence carbon dots (C-dots) were prepared through microwave-assisted carbonization of aqueous starch suspension mediated by sulfuric and phosphoric acids respectively as surface passivating agents. The as-prepared C-dots showed green, blue and yellow luminescence under 365nm UV light. The C-dots were further characterized by UV-Vis, FTIR, and band gap determination. Fourier transform infrared spectroscopy (FTIR) studies revealed bands at 3460 cm^{-1} (OH), 2979 cm^{-1} 1708 cm^{-1} (C=O), 1188 and 1040cm^{-1} (C-O), and 1397 cm^{-1} (C=C) indicative of the graphitic nature of the carbon. The UV-Vis showed blue shifted absorption bands, while the band gap calculated revealed narrow sizing of the C-dots in the semiconductor range. The results suggest that this approach may serve as a facile route to colour tunable photoluminescent C-dot materials with potential biological applications.

Keywords: Carbon quantum dots; Semiconductor; Microwave; Luminescence.
PACS: 78.67.Hc; 72.20.-i; 84.40.-x; 78.55.Mb.

1. Introduction

Carbon dots (C-dots) like other elemental quantum dots (Q-dots) [1] are semiconductor nanocrystals in the size range of 1 to 10 nm. These nanoparticles have size-selective luminescence properties due to their quantum confinement effect and are currently finding increasing interest in optoelectronics, biosensing, bioimaging and medicine [2]. Unfortunately, many of the useful (Q-dots) are of highly toxic elemental composition [2,3]. Carbon-based quantum dots (CQDs or C-dots) are trending as new candidates due to their good solubility and unique optical properties [4, 5], exceptional biocompatibility [3], easy functionalization and their potential as drug delivery vehicles [6] amongst others. All these confer C-dots the edge over metallic semiconductor Q-dots such as CdTe, CdS and PbS [7-10]. Synthetic strategy to obtain C-dots include ‘top-down’ approaches like electrochemical etching, lithography and laser ablation [11–14] etc., and ‘bottom-up’ protocols such as hydrothermal, pyrolytic and microwave carbonization methods [15–18].

Biogenic precursors to C-dots have included sources such as orange juice [16], by thermal processing of bread, caramel, corn flakes and biscuits [19], hydrothermal treatment of pomelo peel for 3 hrs at 200 ^{o}C [20], from ascorbic acid [21] etc. While each of these approaches have their significance, nonetheless it is equally imperative to explore other low-cost and high yield production strategies.

Microwave assisted synthesis is a rapid approach that has been utilized for mostly blue luminescence [22-25] and fewer for other colours [26-27] of C-dots. It is therefore our objective in this study to explore a facile approach to obtain C-dots with tunable photoluminescence (blue, green and yellow) colours. The precursor starch were extracted from four different raw carbohydrate food sources and thereafter carbonized through microwave-assisted treatment in the presence of either sulfuric or phosphoric acids respectively as surface passivating agents.

2. Materials and Methods

2.1. Materials

Carbohydrate sources for starch were; cassava (*Manihot esculenta*), potato (*Solanum tuberosum*), yam (*Dioscorea rotundata*) and rice (*Oryza sativa*). Other reagents include sulphuric acid (H_2SO_4), phosphoric acid (H_3PO_4) (Sigma-Aldrich), sodium hydroxide (NaOH) (BDH) and deionized water. A domestic microwave oven with (2.0 cm) diameter hole drilled into the top.

2.2. Extraction of Starch

Starch was extracted from potato, cassava, rice and yam respectively. In a typical procedure, cassava and yam tubers or potato were peeled, grated and soaked in deionized water for 1hr. Each of the resulting mixtures was stirred and then filtered using cheesecloth to obtain starch suspension that was allowed to stand for 2-3hrs. The supernatant was decanted and the bottom residue air dried to obtain the corresponding powdered starch. Separately, rice starch was obtained by initially pulverizing rice grains to coarse powder using a mortar and pestle. Thereafter, twice the volume of water was added and allowed to soak for about 2 hrs. The mixture was filtered using cheesecloth and further treated as described above to give the dried rice starch powder. The obtained potato, cassava, yam and rice starch powders were used as precursors for C-dot synthesis.

2.3. Microwave Synthesis of Carbon Dots (C-dots)

C-dots were prepared through microwave assisted carbonization of the starch suspensions in water. In a typical procedure, cassava starch powder (1g) was dispersed in 25ml of deionized water in a beaker to give a suspension. Sulphuric acid (7.0 ml, 2M) was added to the starch suspension followed by carbonization under microwave energy at 500W for 3-7 minutes. The colour of the mixture changed progressively from white through light brown and finally to dark brown. The resulting final dark brown mixture was filtered to give a clear filtrate that was kept for further analysis.

Additionally, fresh cassava starch was carbonized after addition of 3.0 ml concentrated phosphoric acid (14.6M) as the surface passivating agent. The reaction mixture also showed similar progressive colour transformation. The final dark mixture obtained was filtered to give a clear filtrate that was kept for further analysis. Rice, potato and yam starches were variously carbonized through similar procedures after addition of sulphuric acid (H_2SO_4) or phosphoric acid (H_3PO_4) as surface passivating agents. The heating regimes were slightly modified to facilitate green and yellow luminescence colours as shown on Table 1. For example, in order to obtain yellow colour with phosphoric acid (H_3PO_4) acid, the carbonization was carried out at 70W-150W for 30-60 minutes. After the colour of the suspension turned to brown, it was then neutralized with 4ml NaOH (5M) solution, before filtration to give a clear solution which was kept for further analysis.

2.4. Characterization of C-Dots

The prepared C-dots were characterized with ultraviolet-visible spectroscopy (UV-Vis) on a $T80^+$ UV-Vis spectrophotometer in the range 200 – 900 nm using distilled water for base line correction. Fourier Transform Infrared spectra (FTIR) were recorded on a BRUKER (vector 22) spectrophotometer over the range of approximately 4000-400 cm^{-1}. Optical band gap were calculated from cut off wavelength values obtained from UV-Vis absorption spectra using the equation below:

$$\text{Band Gap Energy; } (E) = h \times c/\lambda \qquad (1)$$

where E (band gap energy), h (Planck's constant), c (speed of light) and λ (cut off wavelength). The luminescence characteristics of the aqueous filtrates obtained from the carbonization step were investigated by illumination under (365nm) ultra violet (UV) light source in a dark room.

3. Results and Discussion

3.1. Extraction of Starch

The raw carbohydrate food stuffs; potato, cassava, rice and yam utilized in this study as precursor carbon sources are shown in Fig. 1(a-d). Starch powders (Fig. 2a-d) were obtained after processing of the food stuff through peeling, grating (or pulverizing), soaking, filtering, decanting of the supernatant and finally drying of the bottom residue.

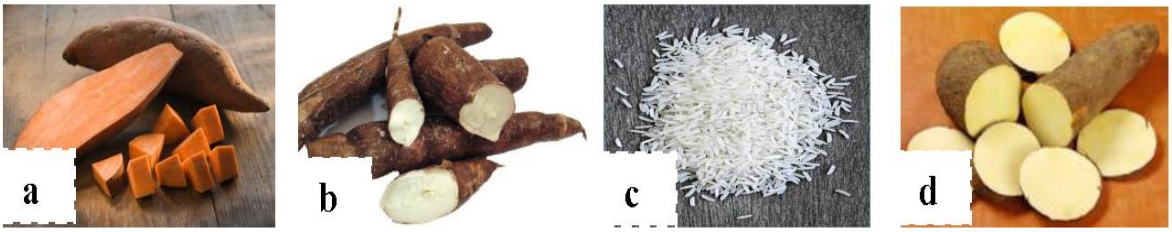

Fig. 1**:** Raw carbohydrate food sources; (a) Potato, (b) Cassava, (c) Rice and (d) Yam.

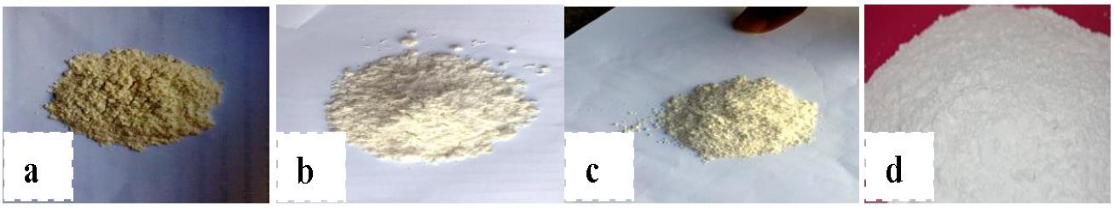

Figure. 2: Starch obtained from; (a) Potato, (b) Cassava, (c) Rice, and (d) Yam.

3.2. Synthesis of C-Dots

The pathway for C-dots synthesis shown in Scheme 1 from the precursor starch is mediated by either H_2SO_4 or H_3PO_4 as surface passivating agents under microwave energy carbonization. The reaction mixture changes from white through light brown and finally to dark brown (Fig 3a-b) to give the filtrate (Fig. 3c). It is envisioned that the starch moiety undergoes hydrolysis to form glucose and fructose which are dehydrated to furfural intermediates and smaller fragmented molecules [28-29]. The intermediates formed then polymerize or aromatize into soluble polymers and aromatic clusters. Furthermore, intermolecular dehydration of the smaller molecules or separation of the aromatic clusters after reaching supersaturation [30-32] facilitates nucleation of the C-dots. Additionally, oxidation introduces functional groups that enhance their water solubility [33].

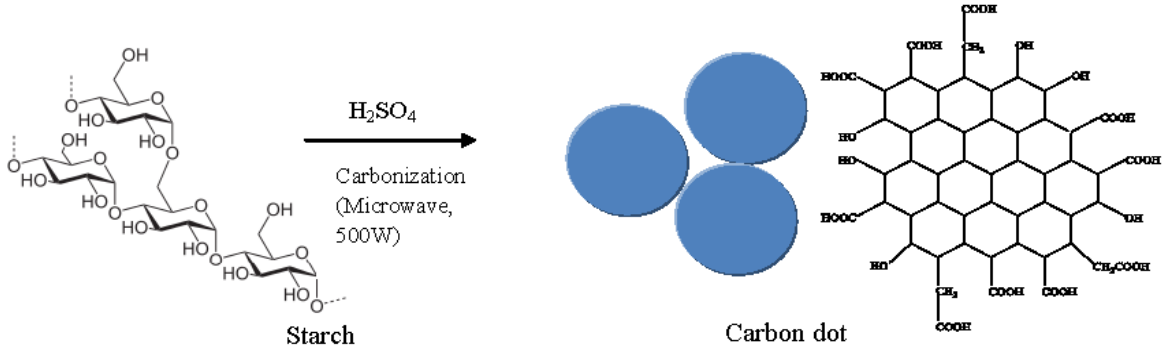

Scheme 1: Synthesis of C-dots from starch.

3.3. Optical Study of the C-Dots

The luminescence properties of the as prepared C-dots solutions were investigated by irradiation with 365 nm UV light. The representative colour in normal light is shown in Fig. 4a, while the characteristic blue, green and yellow luminescence colours are shown in Fig.4b-d. Modification of carbonization protocol on the luminescence characteristics of the C-dots were investigated and presumed to be a function of the heating (wattage), time and the surface passivating agent as highlighted on Table 1.

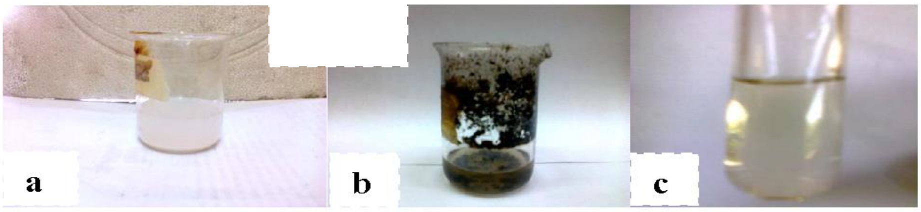

Figure 3: (a) Starch suspension (b) after microwave carbonization (c) solution after filtration.

Sulphuric acid mediated carbonization at 500 W for 3-5 minutes or 5-10 minutes affords blue- or the green-emitting C-dots respectively. It is interesting to note that yellow colour was only obtained by carbonization at lower temperature (70-150 W) albeit for a longer time (30-60 minutes) using phosphoric acid as passivating agent. In this instance however, the reaction mixture is neutralized with a base. The reaction mixture actually showed no luminescence prior to neutralization with NaOH. Consequently, the ability to tune the observed emission colours of the C-dots and their good solubility are desirable characteristics for quantum-dot based candidate probes in biological applications.

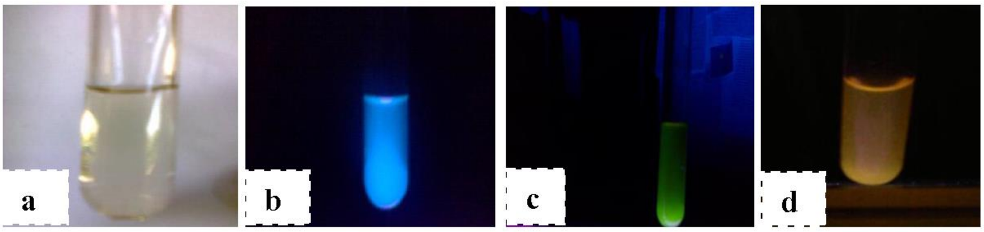

Figure 4: C-dot solutions; (a) under normal light. Under 365 nm UV excitation; (b) blue, (c) green and (d) yellow.

3.4. Fourier Infrared Spectroscopy (FTIR)

The as prepared C-dots were investigated with FTIR spectroscopy particularly to evaluate the functional groups that decorate their edges. In the representative spectrum shown in Fig.5, there is a broad peak centered at 3460cm^{-1} characteristic of the stretching vibrations of a hydroxyl hydrogen bonded O-H. Peaks at 2979 cm^{-1} and 1397cm^{-1} indicate the presence of C-H stretching and C=C stretching vibrations indicative of the graphitic nature of the C-dots [34-35]. The broad peak at 2555cm^{-1} and the strong sharp absorption peak observed at 1708cm^{-1} is associated with O-H and C=O stretching vibrations of carboxyl group. Additionally, there were peaks at 1188 and 1040cm^{-1} assigned to C-O stretching vibrations of carboxyl and hydroxyl groups respectively. The functional groups identified from FTIR analysis corroborate the hydrophilicity and solubility of the C-dots in water.

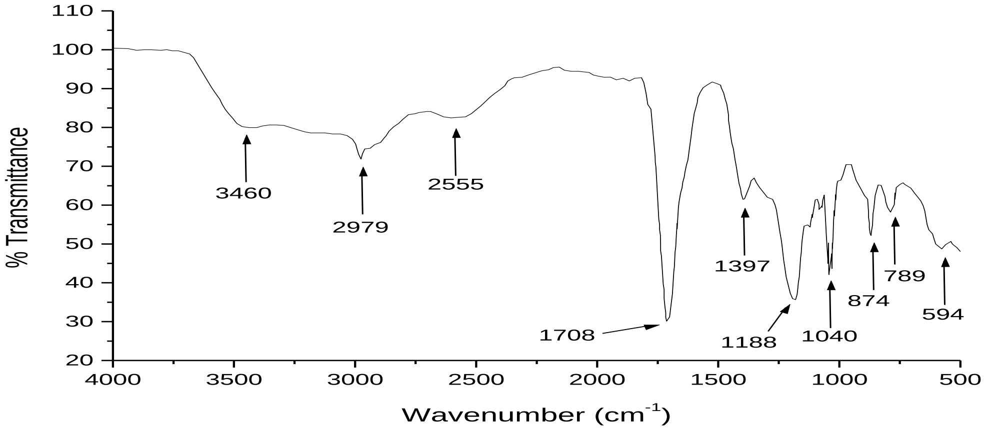

Figure. 5: Infrared spectrum of C-dot

3.5. UV- Vis Absorption Spectra of C-dots

UV-Vis spectra obtained over a scan range of 200 – 900 nm for the blue, green and yellow luminescence C-dots are shown in Fig 6a-c. The absorption maxima fall in the region (190-390) with a tail extending to the visible region [36] were relatively broader for both the green and yellow luminescence colour (Fig. 6b-c), but narrower for the blue C-dots (Fig. 6a). The two patterns may be attributed to non-uniform size distribution in the former while the latter sizes were relatively more uniform. In the representative example, observed maxima were at 233nm, 239nm and 242nm for blue, green and yellow C-dot respectively which were ascribed to the $\pi \rightarrow \pi^*$ transitions of C=C present on C-dots, while the seeming shoulder at 296nm and 302nm for green and yellow (Fig. 6b-c) were due to n $\rightarrow \pi^*$ of carbonyl groups (C=O) [37]. The observed blue shift in the absorption maxima is indicative of a strong confinement with decrease in size [38].

3.6 Band Gap Determination

The band gap energy values of the prepared C-dots were calculated from experimentally obtained UV-Vis absorption spectra cut-off edges [39-40]. The UV-Vis spectra obtained for blue, green and yellow luminescence C-dots (Fig. 6a-c) have strong cutoff wavelengths (λ) at 311 x 10^{-9} m, 347x10^{-9} m and 467x10^{-9} m respectively. The values of the band gap energies (Table 2) obtained using Equation 1 indicates that the C–dots are in the semiconductor range. The blue-luminescence C-dot has relatively higher band gap energy which suggests a much wider energy separation compared to the green and yellow C-dots respectively. This energy separation increases as the size decreases for semiconductor a nanocrystal which is complemented by the shift to the blue end.

Table 1: Reaction conditions for tunable C-dots

S/N	**Source of starch**	**Acid**	**Reaction time (min)**	**Luminescence color under UV light 365 nm**
1	Cassava	2M H_2SO_4	3-5	Blue
2	Potato	2M H_2SO_4	3-5	Blue
3	Rice	2M H_2SO_4	3-5	Blue
4	Yam	2M H_2SO_4	3-5	Blue
5	Cassava	Conc. H_3PO_4	3-7	Blue
6	Potato	Conc. H_3PO_4	3-7	Blue
7	Rice	Conc. H_3PO_4	3-7	Blue
8	Cassava	2M H_2SO_4	5-10	Green
9	Potato	2M H_2SO_4	5-10	Green
10	Rice	2M H_2SO_4	5-10	Green
11	Cassava	Conc. H_3PO_4	30-60	Yellow
12	Potato	Conc. H_3PO_4	30-60	Yellow
13	Rice	Conc. H_3PO_4	30-60	Yellow
14	Yam	Conc. H_3PO_4	30-60	Yellow

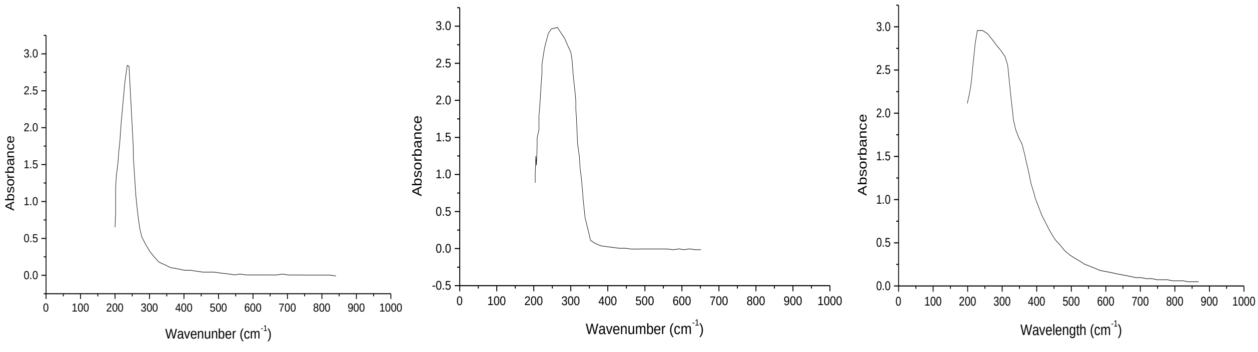

Figure. 6 (a) Blue luminescence C-dots, (b) Green luminescence C-dots, (c) Yellow luminescence C-dot.

Table 2: Calculated Band Gap Energy (E) for the synthesized luminescence C-dots.

Fluorescence C-dots	**Wavelength(nm)**	**Band Gap Energy (eV)**
Blue	311	3.99
Green	347	3.58
Yellow	467	2.66

where 1eV = 1.6×10^{-19} Joules (conversion factor)

4. Conclusion

Tunable luminescence C-dots have been prepared via a facile one-step acidic mediated microwave assisted carbonization of starch precursors (used as carbon source). The approach adopted is simple and cost effective. The result obtained from FTIR studies revealed diagnostic bands for (OH), (C=O), (C-O), and (C=C) that characterize the C-dots. Optical studies show that the luminescence behavior of the C-dots (blue, green or yellow) strongly depends on the reaction conditions. Particularly, the yellow C-dots were obtained only with phosphoric acid passivation at lower reaction temperature after neutralization with base. The band gaps of the C-dots were calculated using cutoff values from UV-Vis and found to fall within the semiconductor range. Finally, the synthesized C-dots exhibited strong luminescence and good solubility which makes them potential materials for probes in biological applications.

References

[1] K. H. Fujioka, M. lruoka, K. Sato, N. M. Manabe, R. lyasaka, S. Hanada, A. Hoshino, R. D. Tilley, Y. Manome, K. Y. Hirakuri, K. Amamoto, Nanotech. **19** (2008) 415102.
[2] L. Xiangyou, W. Hongqiang, S. Yoshiki, P. Alexander, K. Kenji, K. Naoto, Chem. Commun. **47** (2011) 932.
[3] J. Lovric, H. S. Bazzi, Y. Cuie, G. R. A. Fortin, F. M. Winnik, D. Maysinger, J. Molecul. Med. **83** (2005) 377.
[4] X. Xu, R. Ray, Y. Gu, H. J. Ploehn, L. Gearheart, K. Raker, W. A. Scrivens, J. Am. Chem. Soc. **126** (2004) 12736.
[5] S. N. Baker, G. A. Baker, Angew. Chem. Int. Ed. **49** (2010) 6726.
[6] W. Yosufu, H. Aiguo, J. Mater. Chem. C **2** (2014) 6921.
[7] S. C. Ray, A. Saha, N. R. Jana, R. Sarkar, Journal of Physical Chemistry C **113** (43) (2009) 18546.
[8] A. B. Bourlinos, A. Stassinopoulos, D. Anglos, R. Zboril, M. Karakassides, E. P. Giannelis, Small **4** (2008) 455.
[9] Y. Jin-nouchi, T. Hattori, Y. Sumida, M. Fujishima, H. Tada, Chemphyschem. **11** (2010) 3592.
[10] F.A. Kassim, M.A Mahdi, J.J. Hassan, S.K.J. Al-Ani, S.J. Kasim. Int. J. Nanoelectronics and Materials **5** (2012)57.
[11] L. Zheng, Y. Chi, Y. Dong, J. Lin, B. Wang, J. Am. Chem. Soc. **131** (2009) 4564.
[12] L. Cao, X. Wang, M. J. Meziani, F. S. Lu, H. F. Wang, P. J. G. Luo, Y. Lin, B. A. Harruff, L. M. Veca, D. Murray, S. Y. Xie, Y. P. Sun, J. Am. Chem. Soc. **129** (2007) 11318.
[13] A. Yamilov, M. R. Herrera, M. F. Bertino, Nanotech. **18** (2007) 315603.

[14] Y. P. Sun, B. Zhou, Y. Lin, W. Wang, K. A. S. Fernando, P. Pathak, M. J. Meziani, B, A. Harruff, X. Wang, H. F. Wang, P. J. G. Luo, H. Yang, M. E. Kose, B. L. Chen, L. M. Veca, S. Y. Xie, J. Am Chem. Soc. **128** (2006) 7756.

[15] H. Zhu, X. L. Wang, Y. L. Li, Z. J. Wang, F. Yang, X. R. Yang, Chem. Commun. **34** (2009) 5118.

[16] Y. M. Long, C. H. Zhou, Z. L. Zhang, Z. Q. Tian, L. Bao, Y. Lina, D. W. Pang, J. Mater. Chem. **22** (2012) 5917.

[17] S. Sahu, B. Behera, T. Maiti, S. Mohapatra, Chem. Commun. **48** (70) (2012) 8835.

[18] H. Liu, T. Ye, C. Mao, Angew. Chem. Int. Ed. **46** (2007) 6473.

[19]. M. S. Palashuddin, A. Jaiswal, A. Paul, S.S. Ghosh, A. Chattopadhyay, Scientific Reports **2** (2012) 383.

[20] W. B. Lu, X. Y. Qin, S. Liu, G. H. Chang, Y. W. Zhang, Y. L. Luo, A. M. Asiri, A. O. Al Youbi, X. P. Sun, Anal. Chem. **84** (2012), 5351.

[21] X. Jia, J. Li, E. Wang, Nanoscale **4** (2012) 5572.

[22] S. N. Qu, X. Y. Wang, Q. P. Lu, X. Y. Liu and L. J. Wang , Angew. Chem. Int. Ed. **51**(2012) 12215.

[23] Q. Wang, X. Liu, L. C. Zhang and Y. Lv, Analyst **137** (2012) 5392.

[24] D. L. Xiao, D. H. Yuan, H. He and J. R. Lu, Luminescence **28** (2013) 612.

[25] N. Na, T. T. Liu, S. H. Xu, Y. Zhang, D. C. He, L. Y. Huang and J. Ouyang, J. Mater. Chem. B **1** (2013) 787.

[26] S. Chandra, P. Das, S. Bag, D. Laha and P. Pramanik, Nanoscale **3** (2011) 1533.

[27] N. Puvvada, B. N. P. Kumar, S. Konar, H. Kalita, M. Mandal and A. Pathak, Sci. Technol. Adv. Mater. **13** (2012) 045008.

[28] H. Li, H. Ming, Y. Liu, H. Yu, X. He, H. Huang, K. Pan, Z. Kang,S-T. Lee, New J. Chem. **35** (2011) 2666.

[29] W. Kwon, S. Do, S. W. Rhee, RSC Adv. **2** (30) (2012) 11223.

[30] T. Sakaki, M. Shibata, T. Miki, H. Hirosue, N. Hayashi, Bioresource Tech. **58** (1996) 197.

[31] B. Chen, F. Li, S. Li, W. Weng, H. Guo, T. Guo, X. Zhang, Y. Chen, T. Huang, X. Hong,S. You, Y. Lin, K. Zeng, S. Chen, Nanoscale **5** (2013) 1967.

[32] X. Sun, Y. Li, Angew Chem. Int. Ed. **43** (2004) 597.

[33] J. Ryu, Y. W. Suh, D. J. Suh, D. J. Ahn, Carbon **48** (2010) 1990.

[34] R. C. M. De Paula, J. F. Rodrigues, Carbohydr. Polym. **26** (1995) 177.

[35] X. Zi-Qiang, Y. Li-Yun, F. Xiao-Yang, J. Jian-Cheng, M. Jie, P. Wu, J. Feng-Lei, X. Qi, L. Yi, Carbon **66** (2014) 351.

[36] Y. Wang, A. Hu *J. Mater. Chem. C* **2** (2014) 6921.

[37] D. Yongqiang, P. Hongchang, B. Y. Hong, G. Chunxian, S. Jingwei, C. Yuwu, M. L. Chang, Y. Ting, Angew. Chem. Int. Ed. **52** (2013) 7800.

[38] S.B. Rana, A. Singh, S. Singh, Int. J. Nanoelectronics and Materials. **6** (2013) 45.

[39] U.I. Gaya. *Heterogeneous Photocatalysis using inorganic semiconductor solids*, Springer (2014).

[40] J. Dharma, A. Pisal *Simple Method of Measuring the Band Gap Energy Value of TiO_2 in the Powder Form using a UV/Vis/NIR Spectrometer*. PerkinElmer Inc. USA (2009).

LIST OF SYMBOLS

BDH	
CQD	Carbon Quantum Dots

C-dots	Carbon Dots
FTIR	Fourier Transform Infrared
UV	Ultra violet
UV-Vis	Ultraviolet Visible Spectroscopy

Exp. Theo. NANOTECHNOLOGY 1 **(2017)** 23 – 30

Experimental and Theoretical NANOTECHNOLOGY
http://etn.siats.co.uk/

Analysis of flip flop design using nanoelectronic single electron transistor

S. Rajasekaran*, G. Sundari

Faculty of Electronics Engineering, Sathyabama University, Chennai-600119, India
*) *Email: srsekar7@gmail.com.*

Received 3 March 2015; Revised 26 Nov. 2015; Accepted 16 Feb. 2016

Single Electron Transistor (SET) is a nanoelectronic device that operates under the controlled mode of tunneled individual electrons. In this paper, a comparative analysis was performed employing SET based D-Flip flop with conventional logic D-flip flop. SET is eminent nanoscale devices that have low power dissipation, high speed and performance. The flip flop design was simulated using SIMON simulator and the stability of its operation was analyzed applying the Monte-Carlo method that represented stability with low power dissipation and matched the functionality of traditional CMOS devices.

Keywords: Logic circuits; Coulomb blockage; Nanoelectronics; Single electron device.
PACS: 42.79.T; 73.23.Hk; 85.35p; 85.35.Gv.

1. Introduction

The advancement of CMOS technology is still in back evolution and the increase in power utilization has become a main issue in the fabrication of large-scale integrated circuits. Consequently, the single-electron transistor (SET) has intrigued considerable attention because of its low power disbursement and high packing concentration. The information in the form of bits is represented by the presence or absence of single electrons at the quantum conducting islands. The fundamental principle of single-electronics is the Coulomb blockade was first observed and studied by Gorter [1].

It is widely known the size and transistor compactness facilitate vast improvement in the semiconductor based technology. Single-electron tunneling device [2] also has smart features like excellent current control, reduced dimensions and low noise behavior. These features should allow the realization of chips containing a number of the devices orders of magnitude greater than those indicated by the roadmap but still respecting the roadmaps area and power restrictions [3]. A variety of useful devices and concepts utilizing the single-electron tunneling features, such as, cellular automata, the binary decision device [4], and SET logic gates ie. OR, AND, NAND, NOR, etc. [5,6], single electron memories [7], control–control-Not gate [8], analog to digital converter [9], stochastic associative memory [10] have been projected and experienced by actual devices.

The need for computer-aided design and simulation of single-electron circuits has long been recognized. Several simulators and simulation methods have been developed to support single-electron circuit design. SIMON is such a simulator developed by Wasshuber et al [11]. Fabrication of SEDs is an expensive and time-consuming process and, because of that, computer-aided design and simulation tools have been developed in order to study these circuits. A major improvement in SED circuits was achieved by the development of SIMON, which is a Monte Carlo-based tool capable to design, simulate and study SEDs and circuits.Up to date, SIMON has been used for various relevant studies and showed it is a proven tool for such a mission [12].

2. Single-Electron Tunnelling

2.1 Coulomb blockade

Single-electron circuits consist of conducting quantum islands, tunnel junctions, capacitors, and voltage source. The quantum islands are subjectively connected between the tunnel junctions, capacitors and voltage sources. The movement of single electron charge through the tunnel junction is referred as tunnelling, where the electrons are tunnelled through a tunnel junction strictly one after another. This tunnel event of an electron is described by single electronics orthodox theory also a stochastic nature and the energy quantization is in discrete process. If the additional electrons are injected through the energy barrier of the insulating layer, it may prevent the system is said to be Coulomb blockade.

The basic principle of single electronics is that one needs coulomb energy E_C to charge an island with an electron. This energy is:

$$E_C = e^2/2C >> 2k_BT \tag{1}$$

Where C_iC is the capacitance of the island, e is the elementary charge, k_B is Boltzmann's constant and T is the absolute temperature [13]. Since the electric charge flows through the tunnel junctions in multiples of electrons. To assure that electron states are localized on islands all tunnel resistances must be larger than the fundamental quantum resistance

$$R_T > R_Q = h/e^2 \approx 25.813\ K\Omega \tag{2}$$

where h is Planck's constant.

To simulate in a single-electron circuit the tunnel event of electrons from island to island has to determine the rates of all possible tunnel events due to free energy changes. The free energy F, of a single-electron circuit is the differences of the electrostatic energy U, stored in its capacitances and the work done by the voltage sources of the single electron circuit W,

$$F = U - W \tag{3}$$

The electrostatic energy is given by

$$U = \frac{1}{2}(q, v)\left(\frac{V}{Q}\right) \tag{4}$$

where q and v are the unknown variables of the island charge and voltage matrices respectively, and Q and V are the known variables of the island charge and voltage matrices, respectively. The work done by the voltage sources is given by

$$W = \sum \int V_n(t) i_n(t) dt$$
(5)

where $\mathrm{V}_n(\mathrm{t})$ t) is the voltage of the n^{th} voltage source and $\mathrm{i}_n(\mathrm{t})$ t) is the current through the n^{th} voltage source. The tunnel rate r for a particular tunnel event is given by

$$\Gamma = \frac{\Delta F}{e^2 R_r \left[1 - \exp(-\frac{\Delta F}{kT}\right]} \tag{6}$$

where ΔF is the free energy change due to this tunnelling event, R_T is the tunnel resistance on the electron transported through tunnel junction, and k_BT is the thermal energy. Overall tunnel rates for all possible tunnel events is determined using a Monte Carlo method combined with an exponential distribution of tunnel events The time duration of a particular event is given by

$$\Delta t = -\frac{In(r)}{r} \tag{7}$$

2.2. Monte Carlo Technique

Currently, two simulation approaches used in SET circuits. One is based on a Monte Carlo method, and the other on a Master equation Method. The Monte Carlo approach starts with all possible tunnel events, considered to be independent and exponentially distributed. Calculates their probabilities, and chooses one of the possible events randomly, weighted according to their probabilities. The Monte Carlo approach gives better transient and dynamic characteristics of SET circuits because its model the underlying microscopic physics. Tunnel events are modelled as discrete events as long as the electrons are confined on quantum dots.

2.3. Single-Electron Transistor (SET)

Single-electron Transistor is a Nanoelectronic device that used to monitor the electron tunnelling through the quantum island. SET consists of two tunnel junctions and a quantum island (quantum dot) about one nanometer range. The device structure just like MOS transistor, two junctions, as source and drain, instead of channel region the electrons can pass through the quantum island when reaches the coulomb energy. The effect of controlling the electron tunnel is coulomb blockade. The device can transfer the electrons from source to drain one by one under the application of gate voltage. So the tunnelling current is monitored by the voltage applied to the gate through a capacitor. This way charge carrier can transfer across the quantum island only after the sufficient voltage across the capacitor. Electron tunnelling rate based on the stochastic nature of the process takes place across the SET [15].

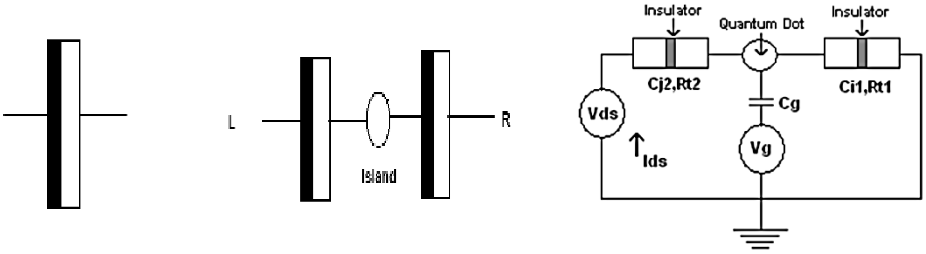

(a) (b) (c)

Figure. 1: (a) Schematic diagram for a tunnel junction, (b) Quantum dot island with two tunnel junctions, (c) Circuit diagram of the Single Electron Transistor.

3. Results and discussion

3.1. Design of D-Flip-flop using Logic gates

The flip-flop is a basic circuit to store state information from two stable states. It is the basic storage element in the sequential logic systems. The design of D-Flip flop circuit using Logic gates is shown in Fig. 2. This circuit is a memory element with two inputs of different logical combination input values. The D-FF consists of 4 NAND gates and one NOT gate, it consists of different logic function.

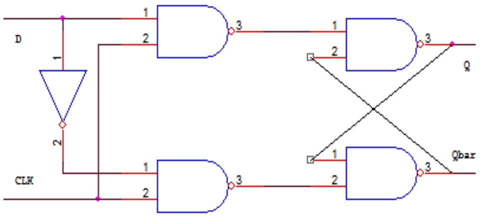

Clock	D	Q
0	x	No Change
1	0	0
1	1	1

(a) (b)

Figure. 2: (a) Diagram of the D-flip flop using Logic gates (b) Logic table.

3.2. Design of D-Flip-flop using SET

The D-Flip flop circuit design using single electron transistor is shown in Fig.3. Hence the circuit comprises thirteen islands, N1 to N13, bounded by eight tunnel junctions. The capacitance of each junction and their resistances are shown in Table 1. The circuit also comprises 7 capacitors, and the values of different for varying nodes. The two voltage sources V_{dd} are constant and its value is 0.16V. The input voltage and clock are applied to the D and Clock respectively through the capacitors C.

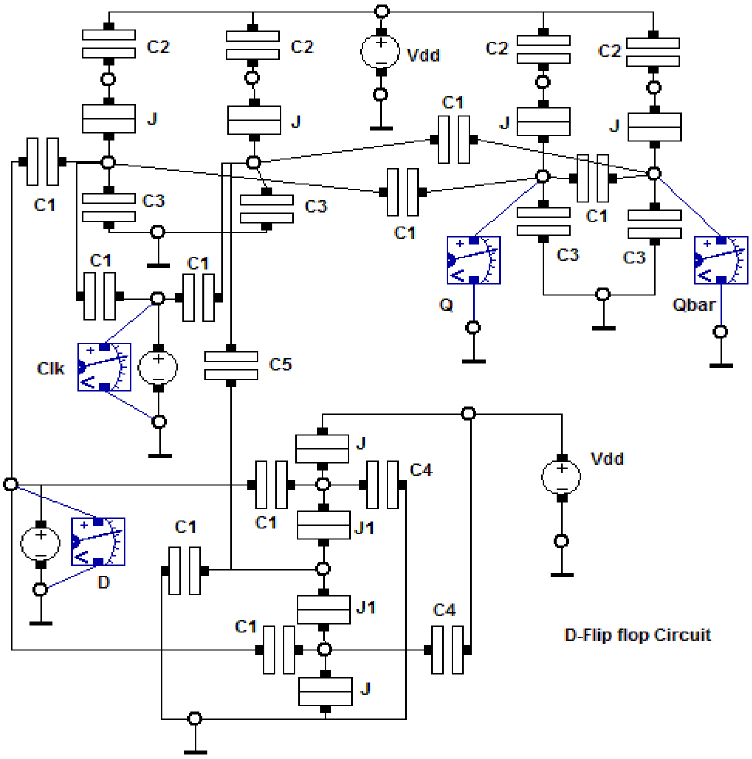

Figure. 3: Circuit diagram of single-electron D Flip flop.

The input voltage and Clock, shown in Fig. 3, are the inputs of the D-Flip flop named as D and Clk, and it takes only two values 0.0V which tends to the logic ‘‘1’’, and -0.1V which tends to the logic ‘‘0’’. The output signals of the D-Flip flop are taken from islands nodes named Q and Qbar respectively.

Table 1: Resistance and Capacitance values of Tunnel Junctions.

Capacitance(F)	**Tunnel Junction(C,R)**	
$C1=5x10^{-18}$	J	$Cj=1x10^{-19}$
$C2= 11.7x10^{-18}$		
$C3=9x10^{-18}$	J1	$Cj1= 5x10^{-18}$
$C4= 4.25x10^{-18}$		
$C5=1x10^{-18}$	$R=1x10^{5}$	

3.3. Analysis of Single-Electron D-Flip flop and Result

The single-electron D-Flip flop needs to be analysed the operational characteristics. From the corresponding output islands we take the outputs Q and Qbar respectively. The presence of zero voltage in the output islands corresponds to logic 1, whereas -0.1V voltage corresponds to logic 0. Hence, the input–output signals, of this D-Flip flop is shown in Fig. 4. The two inputs are D and clock and the two outputs Q and Qbar respectively.

When the input vector [00] is applied an excess electron is transported via tunnelling to island nodes and the island output voltage at Q and Qbar becomes 0.1V. When the input vector and the clock signal are high, the electron tunnels out of nodes are charged according to the Fig. 4 given below.

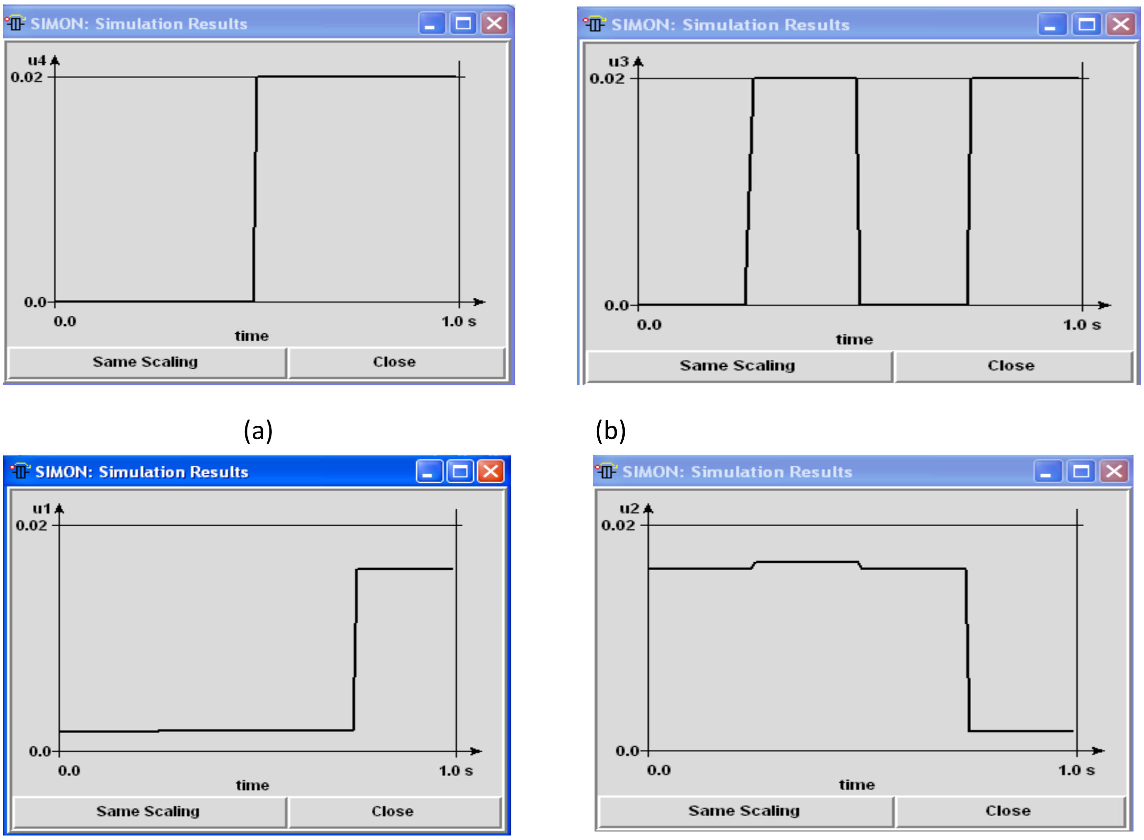

(a) (b)

(c) (d)

Figure. 4. Operation of the single-electron D Flip flop (a) time variation of the input clock CLK; (b) time variation of the input voltage V, (c) time variation of the output charge Q and (d) time variation of the output charge Q-bar.

To confirm the stable operation of flip flop, its stability plot was constructed using SIMON. This plot is shown in figure 5.White regions correspond to completely stable state operation with an integer number of excess or missing electrons on the islands, whereas black regions correspond to completely unstable state operation. The gray regions correspond to less stable regions. The darker the gray region, the more unstable the gate operation. The slight instability in gate operation is apparent in Fig. 5, where slight charge fluctuations are observed.

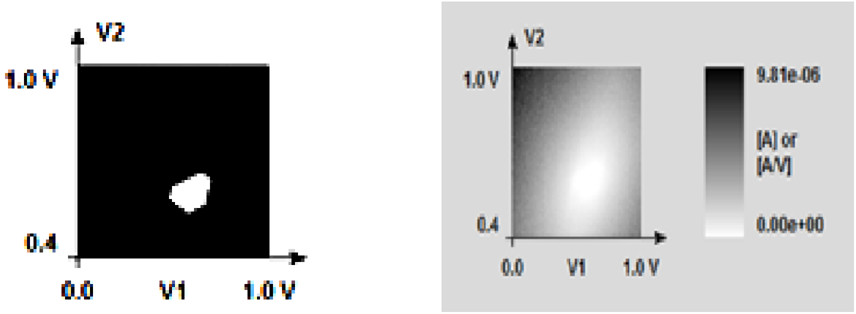

(a) **(b)**

Figure. 5: The stability plots of the single-electron D Flip flop.

5. Conclusions

A single-electron D Flip flop was presented in this paper. This circuit produces their Q and Q-bar. The circuit comprises 8 tunnel junctions, seven capacitors and thirteen islands. Each output is through the island and the presence of positive charge on it corresponds to the logic ‘1’, whereas the absence of charge corresponds to the logic ‘0’. The energy history diagrams were plotted. The simulation procedure and the operational characteristics were verified. The circuit allowed less delay time, and power consumption reduction.

References

[1] K. F. Goser, C. Pacha, A. Kanstein, M. L. Rossmann, Proc. IEEE **85** (1997) 558
[2] Grabert, Hermann, Michel H. Devoret, eds.Single charge tunneling: Coulomb blockade phenomena in nanostructures. **294**. Springer Science & Business Media, (2013)
[3] Likharev, Konstantin K., Proceedings of the IEEE **87** (1999) 606-632
[4] International technology roadmap for semiconductors (2012)
[5] Konstantin K. Likharev. Journal of Nanoelectronics and Optoelectronics, **3** (2008) 203
[6] C. J. Amsinck, N. H. Di Spigna, D. P. Nackashi, P. D. Franzon. Nanotechnology, **16** (2005) 2251
[7] Likharev K K. Hybrid, Proc. of Nanotech **5** (2007) 552
[8] S.H.Jo and W.Lu, IEEE Electron Device Letters **8** (2008) 392
[9] McNeil, R. P. G., et al. Nature **477** (2011) 439
[10] M. Kataoka, M. R. Astley, A. L. Thorn, D. K. L. Oi, C. H. W. Barnes, C. J. B. Ford, D. Andeson, G. A. C. Jones, I. Farrer, D. A. Ritchie, M. Pepper, Phys. Rev. Lett. **102** (2009) 56801
[11] Wasshuber, Christoph, Hans Kosina, and Siegfried Selberherr. Electron Devices, IEEE Transactions on **45** (1998) 2365
[12] Sergey Kubatkin, Andrey Danilov, MattiasHjort, JrmeCornil, JeanLucBrdas, NicolaiStuhr-Hansen, Per Hedegrd, Thomas Bjrnholm. Nature, **425** (2003) 698
[13] U. Hashim, A. Rasmi, S. Sakrani, Int. J. Nanoelectronics and Materials **1** (2008) 21
[14] TsimperidisIoannis, I. Karafyllidis, and AntoniosThanailakis.,Microelectronics Journal **35** (2004) 471
[15] Amit Chaudhry, JatindarNath Roy, Int. J. Nanoelectronics and Materials **4** (2011) 93
[16] AnbarasuPaulthurai, BalamuruganDharmaraj, Microelectronics and Solid State Electronics **4** (2012) 94

[17] Anbarasu.Paulthurai, Balamurugan.Dharmaraj, Int. J. Nanoelectronics and Materials **7** (2014) 149

Exp. Theo. NANOTECHNOLOGY 1 **(2017)** 31 – 40

Experimental and Theoretical NANOTECHNOLOGY
http://etn.siats.co.uk/

Optical properties of manganese chiral single ring by glancing angle deposition technique

Mahsa Fakharpour*

Islamic Azad University, Meybod Branch, Meybod, Iran
**) Email: mahsa.fakharpour@yahoo.com*

Received 25 June 2015; Revised 6 Nov. 2015; Accepted 2 March 2016

Embracing physical vapor deposition system, GLAD method defines the deposition angle, α, in terms of vapor flux and normal substrate. The substrate rotation angle, φ, defines the azimuthal substrate position relative to an arbitrary starting position. We have fabricated periodic nanostructure through utilizing GLAD to control the film deposition conditions over these arrays. Manganese chiral single ring nanostructure have been created using oblique angle deposition method in conjunction with rotation of normal surface substrate. Employing AFM measurement and J-Microvision software, we obtained structure morphology, the size of grains, surface physical roughness and surface void fraction. The optical spectra of the samples were obtained using a single beam spectrophotometer for the incident light of the surface normal. Moreover, it should be mentioned here that Fresnel formulas and experimental measurements of reflectance and absorption spectra could be applied to obtain the refractive index n and the absorption index k. Since Manganese chiral single ring of fabricated nanostructure with GLAD technique is porous, the plot of the refractive index that was observed as a function of the wavelength index aspect has lower values in comparison with homogeneous Manganese thin film associated with longer wavelengths. Therefore, we can control the refractive index of nanostructure with regard to the film density and porous. It is suggested that GLAD may offer an effective method to attain tailor able refractive index.

Keywords: Reflection; Transmission; Absorption; Refractive index.
Keywords: 78.40.Me; 78.20.Ci; 78.20.Ci; 78.20.Ci.

1. Introduction

Metallic nano-structures which depend on their size and geometrical shape have laid the ground for researchers to conduct researches in different fields of application such as biomedicine [1-4], antibacterial [5-8], and optics [9-10]. The Oblique Angle Deposition or Glancing Angle Deposition (OAD and GLAD) method together with rotation of substrate about the substrate surface normal is used to create sculptured nanostructures with pre-designed shapes and desired porosity that can alter different properties at these films.

Owning to the fact that nanostructures of noble metals (gold, silver, and copper) have the ability of exhibiting Localized Surface Plasmon Resonances [11], they have many applications, particularly in the field of Plasmonics [12-16]. Experimental and theoretical investigations have shown that when the number of corners or recesses in the morphology of nanostructure goes up, it can produce higher number of sites to create enhanced fields facilitating Surface Enhanced Raman Spectroscopy (SERS) detection [17].

In 1959, Yong and Kowal used physical vapor deposition to provide helical fluorite films using a rotating substrate as well as the creation of man-made helical structures. They have shown that these thin films could rotate the plan of polarization of normally incident light [18]. Later, Motohiro and Taga that used Oblique Angle Deposition method created the simple chevron films of metal oxides and researched their birefringence properties [19]. In addition, Robbie and Brett prepared the aligned three-dimensional sculptured thin films using a Glancing Angle Deposition (GLAD) technique and studied their optical activity. They have shown that a porous Tio2 helical thin film would select reflection of circularly-polarized light. When the pitch height increased, the reflection band was subsequently shifted to longer wavelength [20,21].

Therefore, the optical properties of helical structures made from materials such as noble metals for example Ag and Au will be expected to be very different from those made from dielectrics [22]. After that, Zhang and Zhao in their paper studied the pitch height-dependent and the polarization angle-dependent optical properties of Ag helical nanostructures [23]. In the current study, we report optical properties such as reflection, transmittance, absorption, and also refractive and absorption indices of Manganese chiral single ring on the glass substrate that was prepared by GLAD method.

2. Experimental details

Prior to being deposited, all glass substrates were ultrasonically cleaned in heated acetone before deposition then ethanol at enough time. Helical nanosculptured thin film on glass substrates were deposited (18 ×18 mm^2 microscope slide) using electron beams in Edwards system (Edward E19 A3) with a base pressure of 2×10^{-8} torr and a deposition rate of 1 $A^{\circ}s^{-1}$ at room temperature. The purity of Manganese was >99.98% and the deposition angle (α°) was fixed at 80°. In order to achieve a uniform deposition on the substrates, a 30 cm distance was chosen between the evaporation source and the substrate and we expected that vapour has a straight trajectories (i.e., without scattering due to the large mean free path ~ 10^3-10^4 cm [24]). Fig1 shows the schematic diagram of the evaporation system associated with the ability substrate rotation for nanosculptured chiral thin films growth. The substrates were fixed on the substrate holder, which was connected to a computer by stepper motor, with 10cm diameter from stainless steel. The substrate holder whose rotation is controlled by previously-written and installed software is rotated about its surface normal with rotation speed of 0.0092rpm during the process of deposition [25]. In this regard, the deposition rate was measured by a quartz crystal deposition rate controller (SQM-160-USA, sigma) that was put close to the substrate and at the same azimuthal angle of substrate. The production of the above-mentioned samples took place by the deposition of Mn on the fixed substrate for a pre-set time with the said deposition rate and then the substrate was rotated continuously until the helical nanostructure with the required thickness was procured. It should not be left unmentioned that the pitch of nanostructure is consistent with the deposition time and deposition rate used [25]. The deposition was carried out with the clockwise rotation of the substrate holder and the helical structures were, therefore, produced with 1 pitch. The diameter of the vertical chirals including the width of rings may be estimated as ≈ 200 nm. It is essential to mention here that we calculated the film thickness (d) or the pitch of the chiral shapes (2Ω) using the tangent rule $\beta = \alpha - sin^{-1}\left(\frac{1-cos(\alpha)}{2}\right), \alpha > 60^{\circ}$ and relation $2\Omega = \frac{2\pi}{\omega} lsin\,(\beta)$ [26]; the thickness of each chiral single ring deposited arranged to be about 400 nm. Furthermore, the surface physical morphology and its roughness were obtained by Atomic Force Microscope (AFM) analysis with a Si tip of 10nm radius in noncontact mode. And last but not east, transmission and reflection spectra of Manganese chiral single ring nanostructure were measured in the wavelength region of 300-2500nm at normal incidence angle using single beam spectrophotometer with 2nm wavelength steps.

To compute the optical constants such as the refractive index (n) and the absorption index (k) of the thin films on the glass transparent substrate at different wavelength, we applied the transmittance and reflectance spectra. As it mentioned about the thin film before, it is the deposited chiral single ring on the glass substrate if the film thickness d and a complex refractive index is given $\hat{n} = n - ik$. The extinction index α (λ) is procured from the experimental measurements of the transmittance T (λ) and reflectance R (λ) and the film thickness d according to the following equation [27]:

$$\alpha = \frac{1}{d} ln\left[\frac{1-R^2}{2T} + \sqrt{\frac{1-R}{4T^2} + R^2}\right] \tag{1}$$

The absorption index k as a function of the wavelength is obtained according to the following equation:

$$k = \frac{\alpha\lambda}{4\pi} \tag{2}$$

Therefore, the refractive index n as a function of the reflectance R (λ) and the absorption index k (λ) is calculated by the Fresnel formula as [28]:

$$n = \left(\frac{1+R}{1-R}\right) + \sqrt{\frac{4R}{(1-R)^2} - k^2} \tag{3}$$

The optical constants n and k were estimated by giving serious consideration to the experimental errors in measuring T (λ) and R (λ) as ∓2%.

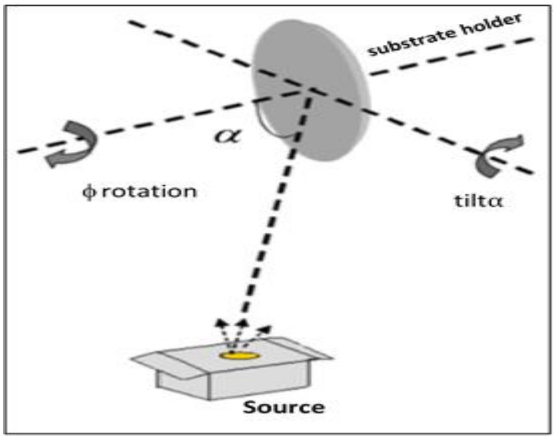

Figure. 1: The schematic of oblique angle deposition in conjunction with rotation of substrate holder

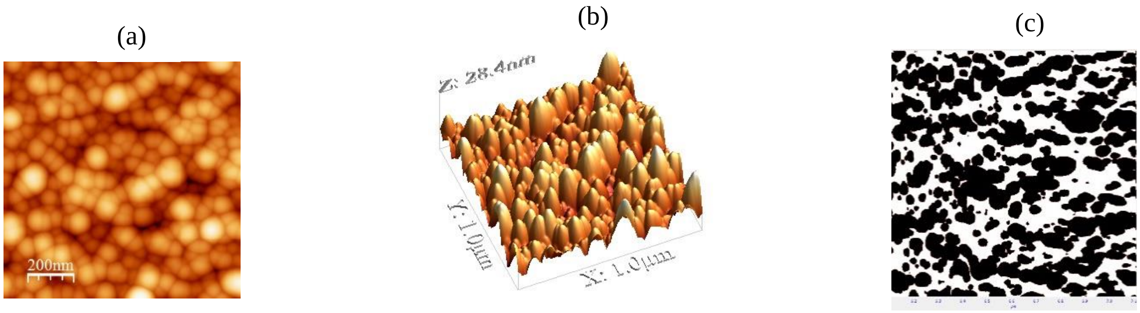

Figure. 2: a) 2D and b) 3D AFM images and c) the surface void image of Manganese chiral single ring.

3. Results and discussion

In Fig. 2, 2D, 3D AFM and the surface void images of Manganese chiral single ring are given in columns a, b and c respectively. The results which we obtained from the 3D AFM images that enabled us to observe the unevenness of the surface are as follows: the size of the grains on the film surface, the surface roughness (unevenness) and the surface void fraction. In addition, it is true to say that the surface of the thin film tends to be rough due to the high diffusion effect and the arriving higher vapour flux. RMS and mean surface roughness of the substrates were measured by AFM and were 5.84 nm and 4.6 nm respectively; diameter of the grains and the surface roughness of the films were measured using the J- Microvision software. We can also obtain the surface void fraction (f_v) using the AFM measurements and a simple program in Matlab software (i.e., white colour_regions in Fig. 2c). This shows that the films prepared with the GLAD methods are the porous films. The quantitative data obtained from the AFM images are given in Table 1.

Table 1. The structural parameters a Mn chiral single ring film

Diameter of the grains (nm)	Surface void fraction (f_v) (%)	Surface roughness (RMS)	Surface roughness (AVG)
83.33	26.50	5.84	4.6

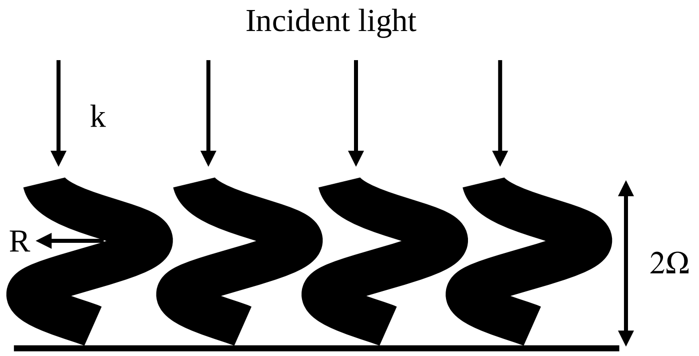

Figure. 3: The schematic for the chiral single ring and the incident light direction.

Figure 3 shows the schematic diagram of a Mn chiral single ring nanostructure. The helical radius R is fixed to be 100 nm and the pitch height is 2Ω. The incident directions are along helical axis, as shown in Fig3. Optical spectra of the Manganese chiral single ring thin film were measured in the wavelength region of 300 to 2500 nm and are given in Figures 4 and 5. Both reflectance and transmittance spectra were measured at the normal incident light.

Table 2 gives the details of both intensity and absorption and reflection peak positions for chiral single ring sample. Given the AFM results, to get the optical measurements such as the experimental absorption, transmittance and reflectance, the following parameters were taken into account:

1- In case of particles whose size is smaller than the wavelength of the incident light, the electromagnetic wave cannot distinguish their structural details, moreover, the small size of particles can be neglected from the scattering contribution. Therefore, regarding the reflection (R) and transmittance (T) spectra, the absorption spectra can be obtained by using the formula (1-R-T). It is to say that the particle size is 83.33 nm in our project, which is smaller than the minimum wavelength of the incident light (i.e., 300 nm).

2- The factors such as the void fraction, surface roughness, the size of grains, and the film thickness are affected by the reflection and absorption spectrum. As it was already shown by several authors [29-31], a smaller grains size, the void fraction, and roughness lead to a rise in reflection. When the size of grains becomes smaller, the density of layer increases and as a result, the void fraction and surface roughness reduces and the surface becomes smoother that results in a rise in the reflection. While the diameter of grains and the fraction of surface void in our work are 83.33 nm and 26.5% alternatively and the RMS and AVG surface roughness are 5.84 nm and 4.6 nm alternatively (Table 1), the reflection increases (around 30%).

3- The reflectance spectra in Fig. 4a show the peaks in UV and visible wavelengths regions. These peaks which are given in Table 2 are about 327, 449, and 880 nm. Fig. 4b shows the wavelength dependence transmittance of nanostructure of Mn chiral single ring. In this regard, Savaloni et al. [32] produce Mn helical structures with square, rectangle and pentagon shapes and showed that the transmittance will considerably increase when wavelengths are larger than the film thickness. It should be noted that the film thickness is about 400nm in this project. Therefore, the transmittance increases as we increase the wavelength, on the other hand, the transmittance spectra becomes constant almost in λ> 1500 nm and does not depend on the wavelength.

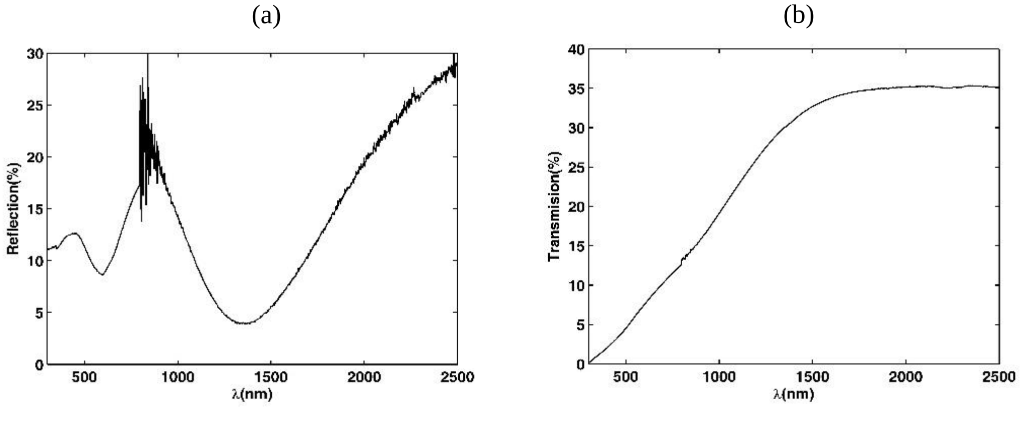

Figure. 4: a) Reflection and b) Transmission spectra of Manganese chiral single ring thin film.

Table 2: The details of both intensity and absorption and reflection peak positions for nano-structure of Mn chiral single ring.

	Wavelength (nm)			**Intensity (%)**		
Reflection	327	449	880	11.21	12.61	18.61
Absorption	300	555	1188	88.77	84.41	68.06

4- Fig. 5 shows the absorption spectra of Mn chiral single ring nanostructure. We may clearly observe two peaks, one at the lower wavelengths (i.e, 555 nm) and the other at the longer wavelengths (i.e, 1188 nm). In addition, one distinguishing the peak at the lower wavelength has the higher intensity of the absorption (Table 2). Siabi and Savaloni [33] show that the optical response of metallic structures that is affected by a limited thickness has no effect on the optical spectra (~320 nm). Therefore, it may be suggested that the optical results discussed in this paper are related to the top 320nm thickness of the film. Hence, considering that the thickness of film in this work is about 400 nm, the light may interact with a complete pitch at the low wavelength. However, when the wavelength increases, the light may not interact with sections of the underlying pitch and may only interact with the top surface of the film. This will decrease the intensity of the absorption spectra. In other words, when the wavelength goes up, the number of particles interacting with the light goes down. It can be observed that the peak at long wavelength has the lower intensity of the absorption.

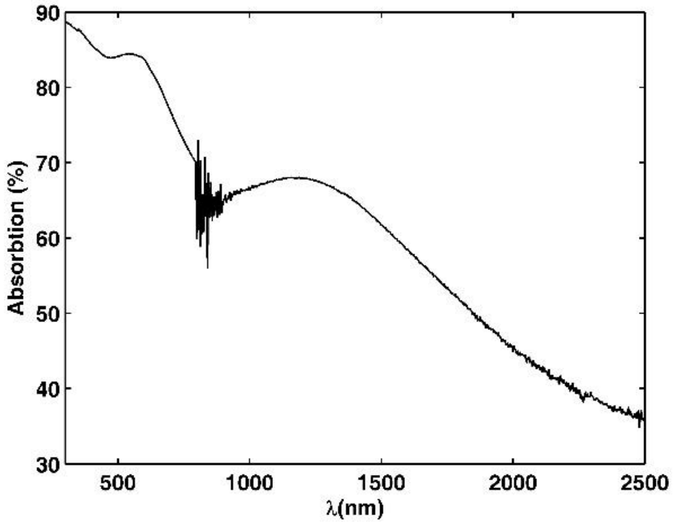

Fig. 5: Absorption spectra of Manganese chiral single ring thin film.

5- Considered as a function of wavelength, the refractive index (n) and the absorption index (k) of Manganese chiral single ring were attained from the experimental results at normal incident light through using the equations (1) to (3) as it was shown in Fig. 6.

Figure 6a shows a plot of k versus wavelength for nano-structure of Manganese chiral single ring. As a function of wavelength, the plot of k changes exponentially while the absorption index does not change significantly in the visible wavelengths region. It should be noted here that the absorption index increases extensively at very long wavelengths.

Wang and et al., prepare nanostructure TiO2 [34] and ZnS [35] thin films by employing angle deposition technique and show that the packing density of films decreases as the incident angle increases. At the flux angle of α=80° and 75°, the packing density and the refractive index decrease. It can be attributed to the porous structure in GLAD films, which will inevitably result in the decrease of the effective refractive index.

In the present paper, the results obtained from the refractive index n of nano-structure of Manganese chiral single ring was compared with the structure of Manganese thin film according to reference [36]. Fig. 6b shows the refractive index n of Manganese thin film and Manganese chiral single ring nanostructure as a function of wavelength in the UV and visible regions of 300 to 1000 nm. The peaks can be observed at about 440 and 860 nm in the optical constant n due to the rise in reflectance of the film in which the refractive indices are 2.043 and 2.560 respectively (Fig. 6b). While indices of Manganese thin film, according to reference [37], are obtained n= 2.102 and 2.941 at the wavelengths 440 and 860 nm respectively. In this work, we report that Manganese chiral single ring nanostructure prepared by GLAD method is the porous structure and its refractive index is lower than that of the thin film at most of the wavelengths. In particular, at the wavelength of 590 nm, the refractive index extensively reduced to 1.345 (Fig. 6b), which is even less than that of Manganese thin film. Hence, the refractive index of the porous nanostructure depends on the wavelength. Therefore, using density and porous of thin film, the GLAD technique can control the refractive index of the nanostructure.

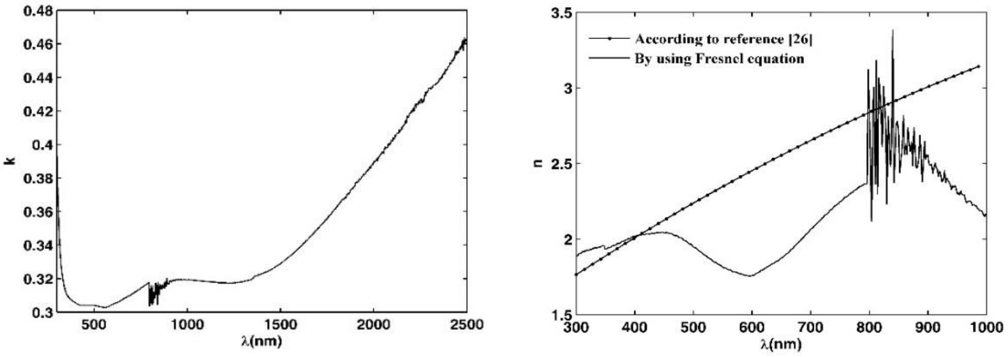
(a)

(b)

Figure. 6: Plot of optical indices of Manganese chiral single ring thin film a) Absorption index and b) Comparison of refractive index n of Manganese thin film according to reference [36] and Manganese chiral single ring nanostructure.

4. Conclusions

In this paper, we reported that Manganese chiral single ring nanostructure prepared by GLAD method is the porous nanostructure. The porosity of thin film is affected by the reflection and absorption spectrum. Using the experimental results R, T, and the Fresnel formula, we obtained the optical constants n and k. While the refractive and absorption indices depend on the wavelength, the absorption index k as a function of wavelength changes exponentially. The refractive indices of Manganese chiral single ring are about n= 2.043 and 2.560 at the wavelengths of 440 and 860 respectively, which are lower than those of the corresponding Manganese thin film because nanostructure of Manganese chiral single ring is the porous nanostructure. Therefore, the GLAD technique can control the refractive index of the nanostructure by density and the porous of thin film.

References

[1] T. Tran, T. Nguyen; Controlled growth of uniform noble metal nanocrystals: Aqueous-based synthesis and some applications in biomedicine, Colloids and Surfaces B: Biointerfaces **88** (2011) 1

[2] P. K. Jain, K. S. Lee, I. H. El-Sayed and M. A. El-Sayed; Calculated Absorption and Scattering Properties of Gold Nanoparticles of Different Size, Shape, and Composition: Applications in Biological Imaging and Biomedicine, J. Phys. Chem. B **110** (2006) 7238.

[3] A. Mahapatro; Bio-functional nano-coatings on metallic biomaterials, Materials Science and Engineering: C **55** (2015) 227

[4] Z. Karimi, L. Karimi, H. Shokrollahi; Nano-magnetic particles used in biomedicine: Core and coating materials, Materials Science and Engineering: C **33** (2013) 2465

[5] J. Arul Mary, J. Judith Vijaya, L. John Kennedy, M. Bououdina; icrowave-assisted synthesis, characterization and antibacterial properties of Ce–Cu dual doped ZnO nanostructures, Optik - International Journal for Light and Electron Optics **45** (2015) 56

[6] K. Ashtari, J. Fasihi, N. Mollania, K. Khajeh; A biotemplated nickel nanostructure: Synthesis, characterization and antibacterial activity, Materials Research Bulletin **50** (2014) 348

[7] S. Pal, Y. K. Tak and J. M. Song; Does the Antibacterial Activity of Silver Nanoparticles Depend on the Shape of the Nanoparticle? A Study of the Gram-Negative Bacterium Escherichia coli, J. M. Appl. and Env. Mic. **73** (2007) 1712

[8] Tariq Jan, Javed Iqbal , Muhammad Ismail, Noor Badshah, Qaisar Mansoor, Aqsa Arshad, Qazi M. Ahkam; Synthesis, physical properties and antibacterial activity of metal oxides nanostructures, Materials Science in Semiconductor Processing **21** (2014) 154

[9] N. M. Ahmed, Z. Sauli, U. Hashim, Y. Al-Douri; Investigation of the absorption coefficient, refractive index, energy band gap, and film thickness for $Al_{0.11}Ga_{0.89}N$, $Al_{0.03}Ga_{0.97}N$, and GaN by optical transmission method, International Journal of Nanoelectronics and Materials **2** (2009) 189

[10] H. Nadir, M. Khudheir, R. Hayfa, M. Hazim ; Electric field distribution in weakly absorbing monolayer at oblique incidence of light, International Journal of Nanoelectronics and Materials **6** (2013) 87

[11] Z. Y. Zhang, Y. P. Zhao; Optical properties of helical Ag nanostructures calculated by discrete dipole approximation method, Appl. Phys. Lett. **90** (2007) 221501

[12] M. Wan , M. Tian, S. Yuan, X. Sun, J.He; Surface plasmon modes of infinite cylindrical metallic nanostructures, Optik - International Journal for Light and Electron Optics **124** (2015) 7036

[13] J. Z. Zhang and C. Noguez; Plasmonic Optical Properties and Applications of Metal Nanostructures, Plasmonics **3** (2008) 127

[14] Z. Y. Zhang and Y. P. Zhao; Optical properties of helical Ag nanostructures calculated by discrete dipole approximation method, Appl. Phys. Lett. 90 (2007) 221501

[15] M. Akhlaghi; Optimization of the plasmonic nano-rods-based absorption coefficient using TLBO algorithm, Optik - International Journal for Light and Electron Optics **126** (2015) 5033

[16] Z. Wang, X. Quan, Z. Zhang, P. Cheng; Numerical studies on absorption characteristics of plasmonic metamaterials with an array of nanoshells, International Communications in Heat and Mass Transfer **68** (2015) 172

[17] K. L. Kelly, E. Coronado, L. L. Zhao, G. C. Schatz; The Optical properties of metal nanoparticles: the influence of size, shape, and dielectric environment, J. Phys. Chem. B **107** (2013) 57

[18] N. O. Young and J. Kowal, Nature (London) **183** (1959) 104

[19] T. Motohiro and Y. Taga, Appl. Opt. **28** (1989) 2466

[20] K. Robbie and M. J. Brett, J. Vac. Sci. Technol. A **15** (1997) 1460

[21] A. C. van Popta, J. C. Sit, and M. J. Brett, Appl. Opt. **43** (2004) 3632

[22] Z. Y. Zhang and Y. P. Zhao, Appl. Phys. Lett. **90** (2007) 221501

[23] Z. Y. Zhang and Y. P. Zhao, APP. Phys. **104** (2008) 013517

[24] L. Eckertova, Physics of Thin Films, chapter 1, Plenum Press, 2nd edition, (1990)

[25] H. Savaloni, F. Babaei, S. Song, and F. Placido; Characteristics of sculptured Cu thin films and their optical properties as a function of deposition rate, App. Sur. Sci. **255** (2009) 8041

[26] H. Savaloni, surface Science of Nanotechnology, Vol. 1, pp. 2671, University of Tehran Press, (2005)

[27] M.M. El-Nahass, A.A.M. Farag, A.A. Atta, Synth. Met. **159** (2009) 589

[28] P.P. Banerjee, Proc. IEEE **73** (2005) 1859

[29] C. Pecharroman, E. D. Gaspera, A. Martucci, R. E. Galindod, P. Mulvaney, J. Phy. Chem. C **119** (2015) 9450

[30] N. D. Singho, N. A. C. Lah, M. R. Johan, R. Ahmad, IJRET **1** (2012) 4

[31] O. Carton, J. Ghaymouni, M. Lejeune, A. Zeinert, Journal of Spectroscopy **2013** (2013) 564

[32] A. Siabi-Garjan, H. Savaloni, " Extinction spectra and electric near-field distribution of Mn nano-rod based sculptured thin films: experimental and discrete dipole approximation results," Journal of Optics **2013** (2013) 45

[33] Araz Siabi-Garjan, Hadi Savaloni, Extinction spectra and electric field enhancement of silver chiral nano-flower shaped nanoparticle; comparison of discrete dipole approximation results with experimental results" Eur. Phys. J. B **86** (2013) 257

[34] S. Wang, G. Xia, H. He, K. YI, J. Shao, Z. Fan, Alloys and Compounds **431** (2007) 286

[35] S. Wang, X. Fu, G. Xia, J. Wang, J. Shao, Z. Fan, App. Surf. Sci. **252** (2006) 8734

[36] E.D. Palik, Handbook of Optical Constants of Solids, Academic, New York (1985)

Exp. Theo. NANOTECHNOLOGY 1 **(2017)** 41 – 48

Experimental and Theoretical NANOTECHNOLOGY
http://etn.siats.co.uk/

Copolysiloxane solvent detector using Langmuir-Blodgett surface potential method

F. L. Supian[1,1], R. Yahaya[2], D. C. K. Lim[3]

[1, 3]*Department of Physics, Faculty of Science and Mathematics, Sultan Idris Education University, 35900 Tanjong Malim, Perak, Malaysia*
[2]*Department of Chemistry, Faculty of Science and Mathematics, Sultan Idris Education University, 35900 Tanjong Malim, Perak, Malaysia*
[1])E-mail: faridah.lisa@fsmt.upsi.edu.my

Received 28 Dec. 2015; Revised 12 Jan. 2016; Accepted 30 Jan. 2016

A quick detection for volatile organic compounds (VOCs), especially in the indoor environment is a must as the build-up level of VOCs is multiple times greater than outdoor environment. By using a surface potential probe, we have analyzed the interaction between copolysiloxane Langmuir-Blodgett (LB) thin films with several commercially used VOCs solvent, specifically chloroform ($CHCl_3$), isopropyl alcohol (IPA) and dichloromethane (DCM). These copolysiloxane LB thin films, namely $P_{50:50}$ and $P_{25:75}$ had been deposited onto aluminium-coated substrates. Subsequently, the surface potential (ΔV) of copolysiloxane LB thin films were monitored during exposure to each solvent. Interaction of these thin films with each solvent produced non-identical changes in ΔV values. In addition, ΔV_{max} value and halftime response for half ΔV_{max} value (t_{50}) were determined. Later, a figure of merit, f was calculated to determine the optimum sensing material per solvent. The most promising candidates particularly as IPA solvent vapour sensors is $P_{50:50}$ copolysiloxanes LB thin film that presented ΔV_{max} (106 mV), smallest halftime response for half ΔV_{max} value achieved, t_{50} (65 s), and considerable f (1.631 mV/s), as compared to others.

Keywords: Langmuir-Blodgett; Surface potential; Organic compounds.
PACS: 68.18.-g; 31.50.-x; 78.40.Me.

1. Introduction

Volatile organic compounds (VOCs) are briefly defined as any compounds that took part in atmospheric photochemical reactions [1]. They are widely used as the solvent in various consumer product and industry manufacturing activities. Excessive usage of these VOC solvents might result in severe health condition as most of these are harmful to human being particularly in vapor form. Polysiloxanes are distinctive hybrid inorganic and semi-inorganic polymers that exhibit high gas permeability, low volatile, good thermal and oxidative stability, high chemical and biocompatibility [2, 3]. These compounds have been used extensively in innumerable applications such as medical, aerospace and sensor [4]. Hence, for the first time, an investigation regarding the interaction of copolysiloxanes, $P_{50:50}$ and $P_{25:75}$ Langmuir-Blodgett (LB) thin films, with several extensively used solvents, namely chloroform ($CHCl_3$), isopropyl alcohol (IPA) and dichloromethane (DCM), have been carried out using a surface potential (NIMA S-POT) probe. This is to verify that these copolysiloxanes might hold the potential to be alternative candidates for VOCs vapor sensing in term of surface potential changes detection.

2. Experimental

2.1 Materials

Two types of copolysiloxanes were selected as the basic materials in this investigation, named $P_{50:50}$ and $P_{25:75}$ as illustrated in Figure 1 and 2. Chloroform from Sigma-Aldrich was used as the solvent to dissolve the copolysiloxanes and produced 0.2 mg/ml of copolysiloxane solutions. Metal evaporation technique prepared aluminium coated-cleaned glass slides acted as the substrates. Three types of common VOCs solvents in the laboratory were chosen, namely $CHCl_3$, IPA and DCM (Figure 3) as the target solvent for interaction with copolysiloxanes. No further purification process required for all the reagents and solvents.

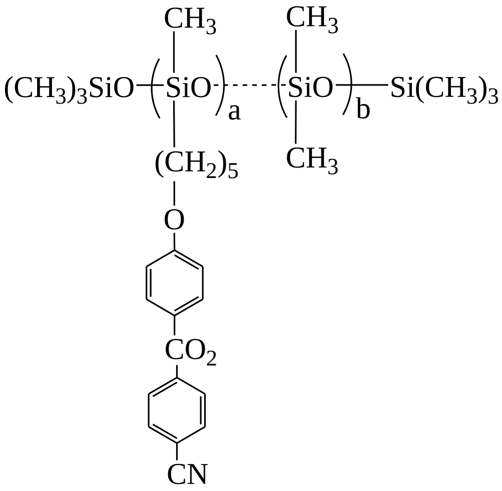

Figure. 1: General structure of copolysiloxanes, $P_{50:50}$ (a:b = 50:50) and $P_{25:75}$ (a:b = 25:75).

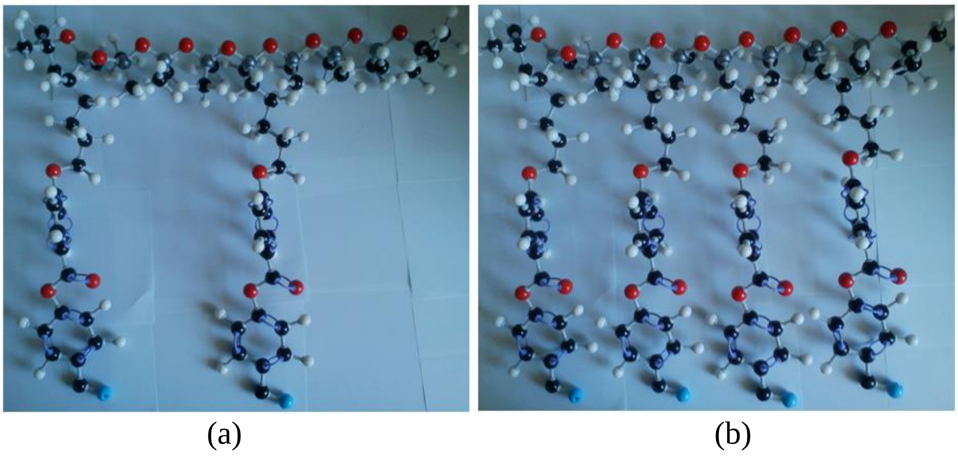

(a) (b)

Figure. 2: Ball and stick models of (a) $P_{50:50}$ and (b) $P_{25:75}$.

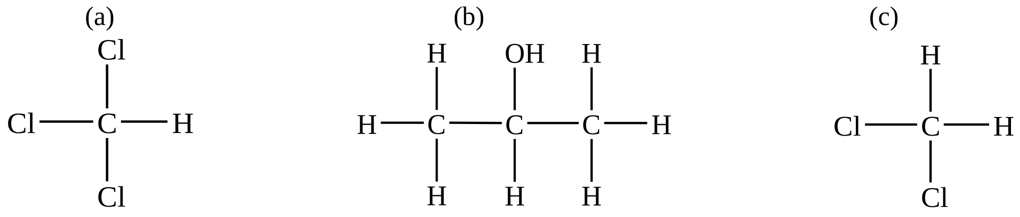

Figure. 3: Chemical structure of (a) $CHCl_3$, (b) IPA and (c) DCM.

2.2 Surface pressure-area isotherm and Langmuir-Blodgett thin films preparation

Surface pressure-area (Π-A) isotherms of copolysiloxanes, $P_{50:50}$ and $P_{25:75}$ were determined using a Langmuir trough (NIMA Model 611). Pure water (Elga Purelab water system, > 15 MΩcm) was utilized as the subphase. Chromatography paper acted as the surface pressure sensor. The solution was dispersed on subphase using a microsyringe. Then, 5 minutes were allowed for solvent evaporation before compression process. The similar procedure applied to the second copolysiloxane solution.

Later, 5 layers of Langmuir-Blodgett (LB) thin film were synthesized through LB deposition technique using the same trough for each copolysiloxanes. Surface pressure, 10 mN/m was selected as the deposition pressure since monolayer formed the compact solid state at this pressure as observed from the isotherm graph. Y-type deposition [4] was performed using 12 mm/min as the compression speed to develop the thin film on a substrate. Subsequently, the developed 5 layers LB thin films were utilized in the surface potential measurement against the VOCs vapor.

2.3 Surface potential measurement

The experiment was conducted in a sealed bag with a dimension of 0.125 m × 0.14 m × 0.095 m to prevent solvent leakage as illustrated in Figure 4.

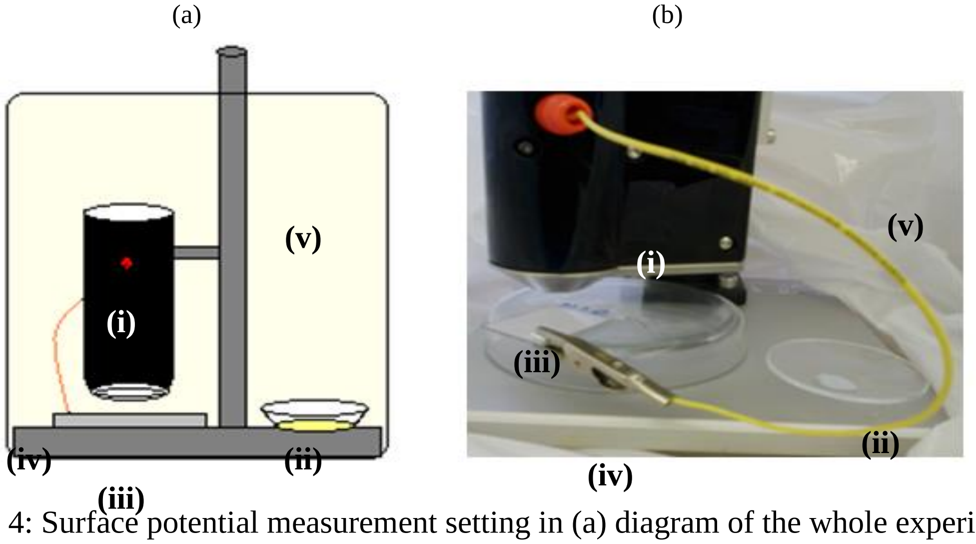

Figure. 4: Surface potential measurement setting in (a) diagram of the whole experimental setup and (b) actual experiment setup. Labels are (i) NIMA S-POT probe, (ii) solvents contained in a watch glass, (iii) LB thin film, (iv) Metal contact and (v) sealed bag.

Surface potential (ΔV) of LB thin films were measured using a S-POT probe (NIMA) with a precision of ± 2 mV attached directly to an Interface Unit software. A vibrating plate of the sensor was placed at a uniform distance (approximately 1 mm) to the LB thin film for ΔV measurement of interaction between copolysiloxane thin film and specific solvent. 1000µl of solvent was injected into the watch glass using a microsyringe from outside of the sealed bag. The duration of exposure time is about half an hour (0 – 2000 seconds) toward the solvents' vapor to determine the ΔV_{max} value and halftime response for half ΔV_{max} value achieved, t_{50} for each type of solvents. All experiments were performed under room temperature (21 ± 0.2 °C).

3. Results and discussion

3.1 Surface pressure (Π-A) isotherm

$P_{50:50}$ and $P_{25:75}$ monolayers were studied through Π-A isotherm graphs that displayed the surface pressure as a function of the molecular area at the air-water interface [5]. In Figure 5, both copolysiloxane formed stable monolayers until the collapse points start to occur at about 12.7 mN/m for $P_{50:50}$ and 19.4 mN/m for $P_{25:75}$. Direct phase transition from liquid expansion phase toward liquid condensed phase (~0 - 3 mN/m for $P_{50:50}$ and ~0 - 2 mN/m for $P_{25:75}$), followed directly by solid state formation (>3 mN/m for $P_{50:50}$ and > 2 mN/m for $P_{25:75}$) were observed. In the solid phase, stretched conformation follows by helical/loop structure conformation was demonstrated. A similar result in [6] proposed that in latter conformation, several functional groups are singled out from the subphase. Hence, 10 mN/m was chosen as the film deposition pressure because more uniform monolayer can be fabricated in stretched conformation than in helical/loop conformation.

The area per copolysiloxane chain was determined by extrapolating the steepest linear gradient of the curve to the x-axis in the solid phase before the area occupied per siloxane unit was calculated. Consequently, the diameter of siloxane unit was determined as an area of a circle was taken on the air-water interface by the siloxane unit. In Table 1, $P_{25:75}$ has a smaller value of area occupied per siloxane unit as compared to $P_{50:50}$ due to coiled and twisted structure of the copolysiloxane backbone, whereas $P_{50:50}$ retain a linear structure. Both copolysiloxane displayed general isotherm characteristics with their own specific signature.

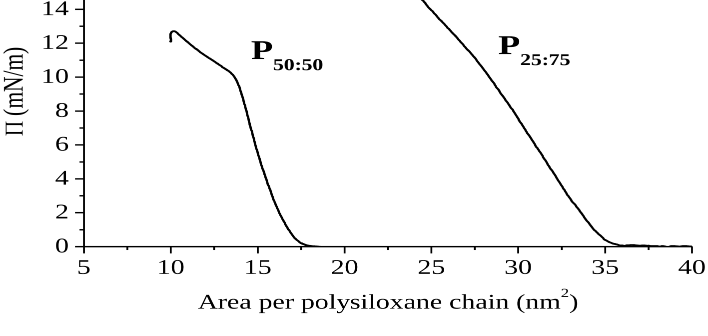

Figure. 5: Isotherm graphs of $P_{50:50}$ and $P_{25:75}$.

Table 1: Data from Π-A Isotherm of copolysiloxane, $P_{50:50}$ and $P_{25:75}$.

Copolysiloxane	**$P_{50:50}$ (50:50)**	**$P_{25:75}$ (25:75)**
Degree of polymerization / Number of repeating units	27	39
No. of unit siloxane	54	156
Limiting area per molecule (nm2)	17	35
Area occupied per siloxane unit (nm2)	0.31	0.22
Estimated siloxane unit size, d (nm)	0.63	0.53

3.2 Maximum surface potential (ΔV) and halftime response (t_{50})

By placing vibrating plate near to the copolysiloxane LB thin film, ΔV was recorded from the alternating current induction flowed in an external circuit due to capacitance changes in the air gap caused by vibration of air [7]. For this work, the ΔV is recorded from 0 s to 2000 s to determine the t_{50} and ΔV_{max} value. The results achieved were visualized in Fig. 6.

Large ΔV values and a quick t_{50} implies good sensor. Thus, a figure of merit, *f* (mV/s), has been formulated to indicate the optimum sensing material per solvent, which is expressed as:

$$f = \frac{\Delta V_{\max}}{t_{50}} \tag{1}$$

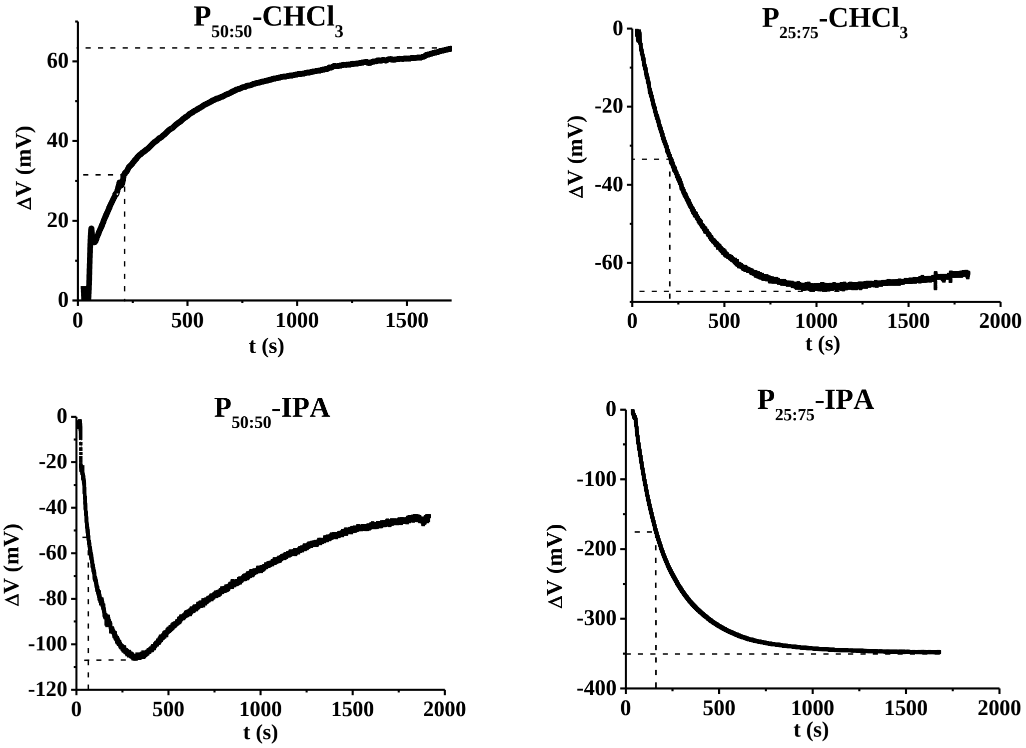

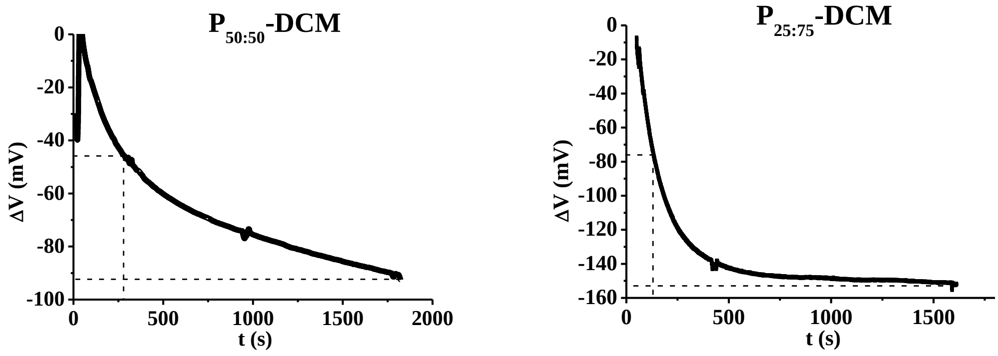

Figure. 6: ΔV and t_{50} for copolysiloxane LB thin films, $P_{50:50}$ and $P_{25:75}$ with $CHCl_3$, IPA and DCM

Table 2: ΔV_{max}, t_{50} and *f* for Copolysiloxanes LB Thin Films, $P_{50:50}$ and $P_{25:75}$ with each 1000µl Solvents.

Copolysiloxanes LB thin film	**$P_{50:50}$**			**$P_{25:75}$**		
	ΔV_{max} (mV)	**t_{50} (s)**	***f* (mV/s)**	**ΔV_{max} (mV)**	**t_{50} (s)**	***f* (mV/s)**
$CHCl_3$	63	210	0.300	67	208	0.322
IPA	106	65	1.631	348	162	2.148
DCM	92	288	0.319	152	134	1.134

Referring to Figure 6 and Table 2, the interaction of these thin films with each solvent produced unlike changes in ΔV values. Moreover, the t_{50} occurred between 65 – 288 s. None of both the copolysiloxanes LB thin films presented overall fast reaction with $CHCl_3$ as their t_{50} were more than 200 s. Both $P_{50:50}$ and $P_{25:75}$ thin films displayed almost similar ΔV_{max} and t_{50}. However, $P_{50:50}$ thin film gave positive changes in surface potential, whilst $P_{25:75}$ thin film displayed negative changes in surface potential as similar to the others in Figure 6.

$P_{50:50}$ thin film displayed the smallest t_{50} (65 s) toward IPA as compared to the others, demonstrated its potential as a sensor for this solvent. Meanwhile, $P_{25:75}$ thin film demonstrated the highest ΔV_{max} (348 mV) and *f* value (2.148 mV/s). This suggests that $P_{25:75}$ thin film still have good interaction with IPA but with a flaw from the aspect of detection time as t_{50} is large (162 s). On the other hands, $P_{25:75}$ thin film displayed better results in DCM as compared with $P_{50:50}$ thin film.

Through *f* values comparison, $P_{25:75}$-IPA showed highest values, followed by $P_{50:50}$-IPA, $P_{25:75}$-DCM, $P_{25:75}$-$CHCl_3$, $P_{50:50}$-DCM and the lowest $P_{50:50}$-$CHCl_3$. The structure of $P_{50:50}$ and $P_{25:75}$ differ only from the cavities in the chain, where $P_{25:75}$ has more cavities compared to $P_{50:50}$. Side chain structures of both copolysiloxanes are identical. Hence, after comparing the three characteristics that demonstrated by thin films with three types of solvents, the $P_{50:50}$ LB thin film was the most encouraging ones to be further studied as a sensor for IPA. However, the selectivity and sensitivity issue is still one of the major challenges in this kind of sensor as both copolysiloxanes can react with all three solvents but with the different results and certainly need to be improved.

4. Conclusion

The ΔV behavior of $P_{50:50}$ and $P_{25:75}$ copolysiloxane LB thin films interaction with several solvents, namely $CHCl_3$, IPA and DCM have been investigated. The results indicated that good interaction and fast time response between $P_{50:50}$ thin film and IPA, proposed a potential one-time use and throw-off type solvent vapour sensor candidate for that specific solvent. This has been strongly supported by the smaller t_{50} = 65 s and f = 1.631 mV/s which indicated the property of optimum sensing material per solvent.

Acknowledgements

F.L.S. acknowledges the University Research Grant from Sultan Idris University of Education (UPSI) and Government of Malaysia for the award of scholarship to conduct this work. The authors are thankful for copolysiloxanes, courtesy of Dr David Lacey's group, Department of Chemistry, the University of Hull for this investigation.

References

[1] United States Environmental Protection Agency, *Volatile Organic Compounds (VOCs)-Technical Overview*. Washington: Retrieved from http://www.epa.gov/iaq/voc_2.html (2012)
[2] J. E. Mark, Some interesting things about polysiloxanes, *Accounts of Chemical Research* **37** (2004) 946
[3] V. Chandrasekhar, *Inorganic and organometallic polymers*. New York: Springer-Verlag Berlin Heidelberg (2005)
[4] O. N. Oliveira Jr, Langmuir-Blodgett films - Properties and possible applications, *Brazilian Journal of Physics* **22** (1992) 60
[5] A. S. Razali, F. L. Supian, S. A. Bakar, T. H. Richardson and N. A. Azahari, The properties of carbon nanotube on novel calixarene thin film, *International Journal of Nanoelectronics and Materials* **8** (2015) 39
[6] S. Mehta, P. Somasundran, O. Yemul and R. Kulkarni, Effect of Modifying Functional Groups on Interfacial Behaviour of Hybrid Silicone Polymers, Paper presented at the National Conference on Polymers, Pune, India, December 17-20 (2006)
[7] R. M. Leblanc and Q. Huo, "Langmuir and Langmuir-Blodgett Films of Proteins and Enzymes," in *Encyclopedia of Surface and Colloid Science*, 2nd ed (Vol. 5). edited by P. Somasundaran, 3233-3260. Boca Raton: CRC Press (2006)

AUTHOR GUIDELINES FOR JOURNAL ARTICLE

Introduction

This document enables the user to have a better understanding of rules and regulations used for writing journals. However, each institute has its own template so it is advised that after writing any journal or publication, refer to your specific institute references for writing journals and publications.

Format

All files should be submitted as a Microsoft Word Document.

Article Length

Articles should usually be between **4000 and 10000 words** in length. This includes all text including references and appendices. Please allow roughly **280 words** for each figure or table.

Article Title

A title of not more than **16 words** is advised.

Article Title Page

An Article Title Page should be submitted alongside each individual article using the template provided.

This should include:

- Article Title
- Author Details (see below)
- Acknowledgements
- Author Biographies
- Structured Abstract (see below)
- Keywords (see below)
- Article Classification (see below)

Author Details

Details should be supplied on the Article Title Page including:

- Full name of each author
- Affiliation of each author, at time research was completed
- Where more than one author has contributed to the article, details of who should be contacted for correspondence
- E-mail address of the corresponding author

Structured Abstract

Authors should supply a structured abstract on the Article Title Page, set out under 4-7 sub-headings:

- Purpose (mandatory)
- Design/methodology/approach (mandatory)

- Findings (mandatory)
- Research limitations/implications (if applicable)
- Practical implications (if applicable)
- Social implications (if applicable)
- Originality/value (mandatory)

Maximum should roughly be **250** words in total (including keywords and article classification.

Keywords

You should provide up to **10 keywords** on the Article Title Page, which encapsulate the principal topics of the paper.

Article Classification

Categorize your paper on the Article Title Page, under one of these classifications:

- Research paper
- Viewpoint
- Technical paper
- Conceptual paper
- Case study
- Literature review
- General review.

Headings

Headings should be concise, with a clear indication of the distinction between the hierarchies of headings.

The preferred format is for first level headings to be presented in bold format and subsequent sub-headings to be presented in medium italics.

Notes/Endnotes

Notes or Endnotes should be used only if absolutely necessary and must be identified in the text by consecutive numbers, enclosed in square brackets and listed at the end of the article.

Research Funding

Authors must declare all sources of external research funding in their article and a statement to this effect should appear in the Acknowledgements section. Authors should describe the role of the funder or financial sponsor in the entire research process, from study design to submission.

Figures

All Figures (charts, diagrams, line drawings, web pages/screenshots, and photographic images) should be submitted in electronic form.

All Figures should be of high quality, legible and numbered consecutively Graphics may be supplied in color to facilitate their appearance on the online database.

- Figures created in Microsoft Word, Microsoft PowerPoint, Microsoft Excel and Illustrator should be supplied in their native formats. Electronic figures created in other applications should be copied from the origination software and pasted into a blank Microsoft Word document or saved and imported into an Microsoft Word document or alternatively create a .pdf file from the origination software.
- Figures which cannot be supplied in as the above are acceptable in the standard image formats which are: .pdf, .ai, and .eps. If you are unable to supply graphics in these formats then please ensure they are .tif, .jpeg, or .bmp at a resolution of at least 300dpi and at least 10cm wide.
- To prepare web pages/screenshots simultaneously press the "Alt" and "Print screen" keys on the keyboard, open a blank Microsoft Word document and simultaneously press "Ctrl" and "V" to paste the image. (Capture all the contents/windows on the computer screen to paste into Microsoft Word, by simultaneously pressing "Ctrl" and "Print screen".)

Photographic images should be submitted electronically and of high quality. They should be saved as .tif or .jpeg files at a resolution of at least 300dpi and at least 10cm wide. Digital camera settings should be set at the highest resolution/quality possible.

Tables

Tables should be typed and included in a separate file to the main body of the article. The position of each table should be clearly labelled in the body text of article with corresponding labels being clearly shown in the separate file.

Ensure that any superscripts or asterisks are shown next to the relevant items and have corresponding explanations displayed as footnotes to the table, figure or plate.

References

References to other publications must be in Harvard style and carefully checked for completeness, accuracy and consistency. This is very important in an electronic environment because it enables your readers to exploit the Reference Linking facility on the database and link back to the works you have cited through CrossRef.

You should cite publications in the text, for example: (Adams, 2006) using the first named author's name or (Adams and Brown, 2006) citing either names of two, or (Adams et al., 2006), when there are three or more authors. At the end of the paper a reference list in alphabetical order should be supplied:

References for Books

For books you should follow below template:

Surname, Initials (year), Title of Book, Publisher, Place of publication.

References for Book Chapters

For book chapters you should follow below template:

Surname, Initials (year), "Chapter title", Editor's Surname, Initials, Title of Book, Publisher, Place of publication, pages.

e.g. Calabrese, F.A. (2005), "The early pathways: theory to practice – a continuum", in Stankosky, M. (Ed.), Creating the Discipline of Knowledge Management, Elsevier, New York, NY, pp. 15-20

References for Journals

For journals you should follow below template:

Surname, Initials (year), "Title of article", Journal Name, volume, number, pages.

e.g. Capizzi, M.T. and Ferguson, R. (2005), "Loyalty trends for the twenty-first century", Journal of Consumer Marketing, Vol. 22 No. 2, pp. 72-80.

References for Published Conference Proceedings

For journals you should follow below template:

Surname, Initials (year of publication), "Title of paper", in Surname, Initials (Ed.), Title of published proceeding which may include place and date(s) held, Publisher, Place of publication, Page numbers.

e.g. Jakkilinki, R., Georgievski, M. and Sharda, N. (2007), "Connecting destinations with an ontology-based e-tourism planner", in Information and communication technologies in tourism 2007 proceedings of the international conference in Ljubljana, Slovenia, 2007, Springer-Verlag, Vienna, pp. 12-32.

References for Unpublished Conference Proceedings

For unpublished conference proceedings you should follow below template:

Surname, Initials (year), "Title of paper", paper presented at Name of Conference, date of conference, place of conference, available at: URL if freely available on the internet (accessed date).

e.g. Aumueller, D. (2005), "Semantic authoring and retrieval within a wiki", paper presented at the European Semantic Web Conference (ESWC), 29 May-1 June, Heraklion, Crete, available at:http://dbs.uni-leipzig.de/file/aumueller05wiksar.pdf (accessed 20 February 2007).

References for Working Papers

For Working Papers you should follow below template:

Surname, Initials (year), "Title of article", working paper [number if available], Institution or organization, Place of organization, date.

e.g. Moizer, P. (2003), "How published academic research can inform policy decisions: the case of mandatory rotation of audit appointments", working paper, Leeds University Business School, University of Leeds, Leeds, 28 March.

References for Encyclopedia Entries (no author or editor)

For encyclopedia entries you should follow below template:

Title of Encyclopedia (year) "Title of entry", volume, edition, Title of Encyclopedia, Publisher, Place of publication, pages.

e.g. Encyclopaedia Britannica (1926) "Psychology of culture contact", Vol. 1, 13th ed., Encyclopaedia Britannica, London and New York, NY, pp. 765-71.

References for Newspaper Articles (non-authored)

For Newspaper Articles you should follow below template:

Newspaper (year), "Article title", date, pages.

e.g. Daily News (2008), "Small change", 2 February, p. 7.

References for Electronic Sources

If it is available online, the full URL should be supplied at the end of the reference, as well as a date that the resource was accessed.

e.g. Castle, B. (2005), "Introduction to web services for remote portlets", available at: http://www-128.ibm.com/developerworks/library/ws-wsrp/ (accessed 12 November 2007).

Standalone URLs, i.e. without an author or date, should be included either within parentheses within the main text, or preferably set as a note (Roman numeral within square brackets within text followed by the full URL address at the end of the paper).

==

For more information
Contact us:
The Scientific Institute for Advanced Training and Studies
Email: publisher@siays.co.uk
Phone: (0060) 11 113 331 80
WhatsApp & viber
Facebook: https://www.facebook.com/siats.mutamd?ref=bookmarks
Experimental and Theoretical NANOTECHNOLOGY
http://etn.siats.co.uk
Guidelines link: http://www.siats.co.uk/author-guidelines-for-journal-article/

Content